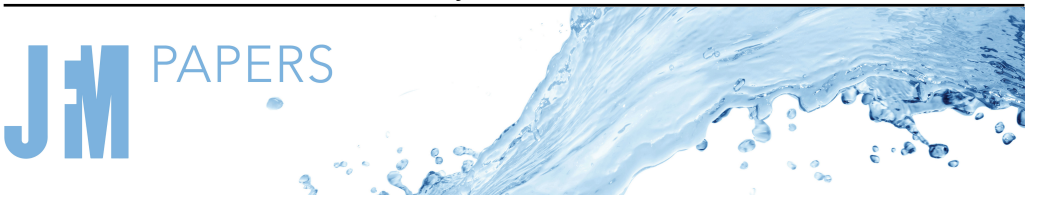
*J. Fluid Mech.* (2025), *vol.* 1008, A9, doi:10.1017/jfm.2025.178




# Instability at imploding gas layer impacted by convergent shock

**Juchun Ding**[1,2], **Chengshuo Fan**[1], **Zhangbo Zhou**[1] and **Xisheng Luo**[1]

[1]Department of Modern Mechanics, University of Science and Technology of China, Hefei 230026, PR China

[2]Laoshan Laboratory, Qingdao 266237, PR China

**Corresponding author:** Zhangbo Zhou, zbzhou@ustc.edu.cn

(Received 5 September 2024; revised 7 January 2025; accepted 3 February 2025)

This work reports high-fidelity shock-tube experiments on the convergent Richtmyer–Meshkov (RM) instability at a heavy gas layer. The convergent shock tube is designed based on shock dynamics theory, significantly mitigating interface deceleration and reflected shock. As a result, long-term observation of instability growth up to nonlinear stage, free of interface deceleration and reshock, is achieved. Various types of $SF_6$ layers surrounded by air with controllable thicknesses and shapes, created using a soap film technique, are examined. For thick layers, the evolutions of the outer and inner interfaces are nearly decoupled regardless of the layer shape. The weakly nonlinear model of Wang (*Phys. Plasmas,* vol. 22, 2015, p. 082702), designed for cylindrical RM instability at a single interface, provides a reasonable prediction of perturbation growth at the inner interface, while slightly underestimating instability growth at the outer interface, as it neglects the effects of rarefaction wave. For thin layers, perturbation growth is fastest at either interface when both interfaces initially possess in-phase perturbations, moderate when only one interface is initially perturbed and slowest when the two interfaces have anti-phase perturbations. This variation in growth rates is due to the fact that the evolution of a thin layer is influenced by both reverberating waves and interface coupling, with each factor being highly sensitive to the layer shape. The original vortex method is extended to address the convergent RM instability by incorporating the influences of unsteady background flow, interface coupling and reverberating waves into the transport of a vortex sheet. This extended vortex method enables accurate prediction of convergent RM instability at a gas layer, covering the full range from early linear to late nonlinear stages.

**Key words:** shock waves, shear-flow instability

© The Author(s), 2025. Published by Cambridge University Press.



https://doi.org/10.1017/jfm.2025.178 Published online by Cambridge University Press

## 1. Introduction

As a shock wave collides with a perturbed interface separating two fluids of different properties, initial perturbations on the interface first grow linearly with time, then nonlinearly, accompanied by the formation of bubbles (a light fluid rises into a heavy one) and spikes (a heavy fluid penetrates into a light one), potentially leading to a transition to turbulent mixing. This type of hydrodynamic instability is generally referred to as the Richtmyer–Meshkov (RM) instability (Richtmyer 1960; Meshkov 1969). A similar yet distinct hydrodynamic instability is the Rayleigh–Taylor (RT) instability (Rayleigh 1883; Taylor 1950), which occurs as the interface suffers continuous acceleration. Unlike the RT instability, which develops only when acceleration is directed from a lighter fluid to a heavier one, the RM instability occurs regardless of the direction of acceleration. Over the past decades, the RM instability has received widespread attention due to its fundamental significance in academic research, such as compressible turbulence (Mohaghar *et al.* 2019; Groom & Thornber 2021) and vortex dynamics (Peng *et al.* 2021), as well as its essential role in engineering applications such as inertial confinement fusion (ICF) (Lindl *et al.* 2014; Betti & Hurricane 2016) and supersonic combustion (Urzay 2018). One of the driving mechanisms of RM instability is baroclinic vorticity, which arises at the interface due to the misalignment between the pressure gradient across the shock wave and the density gradient at the interface (Brouillette 2002).

Previous studies on RM instability focused mainly on the planar shock-induced case (i.e. planar RM instability) (Brouillette 2002; Ranjan *et al.* 2011; Zhou 2017*a*,*b*) and only few exceptions were dedicated to the RM instability induced by a convergent shock (i.e. convergent RM instability) (Fincke *et al.* 2004; Hosseini & Takayama 2005; Vandenboomgaerde *et al.* 2018). A major reason is that geometric convergence poses significant challenges to experiments (Luo *et al.* 2015; Biamino *et al.* 2015), simulations (Lombardini *et al.* 2014*a*,*b*; Li *et al.* 2021; Yan *et al.* 2022) and theoretical analyses (Liu *et al.* 2012; Wang *et al.* 2015). Compared with the planar RM instability, the convergent counterpart involves an initial setting more relevant to ICF, making its study of greater practical importance. In addition to the mechanisms present in planar RM instability (i.e. baroclinic vorticity and pressure disturbance), the convergent RM instability introduces additional factors such as geometric contraction, interface deceleration and the second impact of a reflected shock (Ligrani *et al.* 2020; Wu *et al.* 2024), resulting in much more complex instability growth compared with the planar case.

Early analyses by Bell (1951) and Plesset (1954) showed that the motion of a perturbed interface in cylindrical or spherical geometry, even with a constant velocity, can continuously alter the perturbation growth rate. This phenomenon, known as the geometric contraction effect, has been confirmed by experiment (Ding *et al.* 2017*b*; Lei *et al.* 2017; Luo *et al.* 2019). Also, existing studies have shown that in convergent RM instability, the interface undergoes evident deceleration as it approaches the geometric centre, leading to either RT instability or stability (Lombardini *et al.* 2014*a*; Ding *et al.* 2017*b*; Luo *et al.* 2018). Subsequently, the interface is re-accelerated by a reflected shock. This deceleration and subsequent reshock can significantly complicate the development of the instability (Lanier *et al.* 2003; Lombardini *et al.* 2014*b*; Ding *et al.* 2017*b*; Luo *et al.* 2018). Moreover, in engineering applications such as ICF, there exist two concentric interfaces separating three material layers: the outer ablator, the middle solid deuterium–tritium (DT) shell and the inner gaseous DT fuel. The presence of two (or multiple) interfaces not only introduces interface coupling effect (Jacobs *et al.* 1995; Mikaelian 1995), but also generates complex waves reverberating between the interfaces, further complicating instability growth (Henry *et al.* 2014). So far, the influences of interface coupling and reverberating waves on the convergent RM instability have never been thoroughly examined experimentally, primarily



https://doi.org/10.1017/jfm.2025.178 Published online by Cambridge University Press

due to the significant challenges posed by their interaction with other factors such as interface deceleration and reshock. To gain a clearer understanding of the individual effects of interface coupling and reverberating waves on instability growth from linear to nonlinear stages, it is essential to conduct high-fidelity experiments on a long-term, uniformly imploding gas layer with two interfaces, free from interface deceleration and reshock. This motivates the present study.

Numerous theoretical models have been proposed to predict the RM instability from linear to nonlinear stages under the assumption of incompressible, irrotational and inviscid flow (Richtmyer 1960; Zhang & Sohn 1997; Goncharov 2002; Sohn 2003; Zhang *et al.* 2018*a*). Additionally, substantial theoretical studies have focused on the compressible solutions of linear RM instability for both reflected shock and reflected rarefaction cases, offering in-depth insights into the compressible stage of RM instability (Yang *et al.* 1994; Velikovicha 1996; Wouchuk & Nishihara 1997). Most existing models are designed for planar RM instability, with only a few exceptions addressing the convergent counterpart. Bell (1951) and Plesset (1954) were the first to analyse the amplitude growth of a single-mode interface subjected to arbitrary radial motion in cylindrical and spherical geometries within the linear regime. As the perturbation amplitude becomes comparable to wavelength, nonlinearity becomes pronounced, dramatically increasing the complexity of the problem. Several attempts have been made to predict the nonlinear growth of convergent RM instability using perturbation expansion methods. A fourth-order weakly nonlinear solution for the evolution of a single-mode interface at a fixed radial position in cylindrical geometry was derived by Liu *et al.* (2012). The validity range of the model was then extended to the fully nonlinear stage by using the Padé approximation (Liu *et al.* 2014). Later, Wang *et al.* (2015) obtained a weakly nonlinear solution for the evolution of a uniformly imploding or exploding single-mode interface in cylindrical geometry. These high-order models are suitable only for instability growth at a single interface. For RM instability at two or multiple interfaces, additional factors such as interface coupling and reverberating waves come into play, which are challenging to incorporate into existing models. Additionally, existing high-order models are applicable only up to the weakly nonlinear stage, before the interface exhibits significant roll-ups. However, the convergent RM instability has been found to exhibit stronger nonlinearity compared with its planar counterpart (Luo *et al.* 2019), which limits the applicability of these models. Due to these limitations, there is currently no reliable model capable of predicting the evolution of convergent RM instability at multiple interfaces from early linear to late nonlinear stages. Therefore, developing a new approach to predict convergent RM instability, accounting for complex factors such as reverberating waves, interface coupling and strong nonlinearity, is highly desirable.

In this work, we will first conduct high-fidelity experiments on the convergent RM instability at an $SF_6$ layer surrounded by air in a novel convergent shock tube, designed to eliminate interface deceleration and reshock. Long-term observation of various types of $SF_6$ layers with controllable thicknesses and shapes, subjected to a cylindrical convergent shock, is achieved. By comparing experimental results across different layers and an isolated single-mode interface, the effects of reverberating waves and interface coupling, as well as their dependence on initial conditions, are revealed and explored. The vortex method, originally developed for Kelvin–Helmholtz (KH) and RT instabilities, is extended to model convergent RM instability by incorporating unsteady background flow, interface coupling and reverberating waves into the transport equation for vortex sheet strength. The accuracy of this extended vortex method is validated against experimental results. The results demonstrate the first successful prediction of convergent RM instability at multiple interfaces, spanning from linear to nonlinear stages. These advancements not



https://doi.org/10.1017/jfm.2025.178 Published online by Cambridge University Press

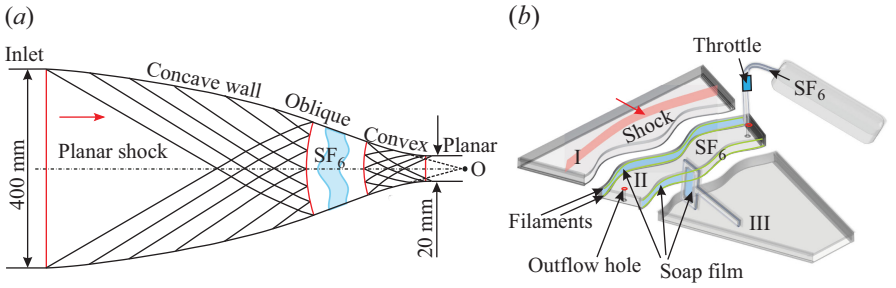



Figure 1. (*a*) Sketch of the curved part of the convergent shock tube. (*b*) A drawing of the interface-formation device.

only deepen our understanding of the mechanisms underlying convergent RM instability, but also provide a reliable framework for predicting instability growth under complex conditions.

The present study deviates from classical RM instability in two key aspects. First, unlike the traditional single-interface configuration, our set-up involves a finite-thickness gas layer with two interfaces, introducing additional complexities such as interface coupling and reverberating waves between the interfaces. This multi-interface arrangement better represents practical applications like ICF, distinguishing it from our previous studies that primarily focused on convergent RM instability at a single interface (Ding *et al.* 2017*b*; Luo *et al.* 2019; Xu *et al.* 2023). Second, this work employs a convergent geometry rather than a planar one, sharing conceptual similarities with the Vishniac–Ryu configuration (Vishniac 1983; Ryu & Vishniac 1987) regarding the shock stability in convergent geometry. However, our approach incorporates several crucial innovations in the shock tube design, distinguishing it from our previous work that used a semi-annular shock tube, where interface deceleration and reshock are unavoidable (Ding *et al.* 2017*b*,2019; Li *et al.* 2020).

## 2. Experimental methods

The convergent shock wave is generated in a horizontal shock tube designed based on shock dynamics theory. A sketch of the curved section of the shock tube is shown in figure 1(*a*). The shock tube has a smoothly curved concave–oblique–convex wall profile, which is carefully designed to modify the shape of an incident planar shock. Specifically, a concave segment initially transforms the incident planar shock into a cylindrical one. This cylindrical shock then travels along the oblique wall, with its strength increasing gradually due to convergence. Subsequently, it is transformed back into a planar shock by a convex wall. Finally, the planar shock exits the end of the shock tube without reflection. The current design prevents shock focusing and reflection at the geometric centre such that interface deceleration and the second impact of the reflected shock, which are unavoidable in previous experiments, can be largely mitigated (Luo *et al.* 2019; Xu *et al.* 2023). This enables long-term observation of instability growth up to the late nonlinear stage, free from the influences of the RT effect and reshock. For further details on the design principles of the curved walls, readers are referred to Zhai *et al.* (2010) and Zhan *et al.* (2018).

A soap film technique, originally developed to create well-characterised single-mode interfaces free of short-wavelength perturbations, diffusion layer and three-dimensionality in planar geometry, is extended in this work to generate various types of $SF_6$ layers in a convergent test section. As depicted in figure 1(*b*), the gas layer is formed in a device



https://doi.org/10.1017/jfm.2025.178 Published online by Cambridge University Press

composed of sections I, II and III. These three sections are made up of transparent acrylic plates (3.0 mm thick) sculpted by a high-precision engraving machine. Four grooves (0.75 mm deep and 0.5 mm wide), matching the desired shapes of the gas layer, are engraved on the inner surfaces of the upper and lower plates of section II. Four thin filaments (1.0 mm thick and 0.5 mm wide), corresponding to the shapes of the grooves, are then inserted into these grooves to create constraints. The protrusion height of the filaments into the test section is less than 0.3 mm, ensuring a negligible influence on the interface evolution (Wang *et al.* 2023). When a square frame dipped with a moderate amount of soap solution (60 % distilled water, 20 % sodium oleate and 20 % glycerine) is pulled along the filaments on both sides of section II, a gas layer with two soap film boundaries is immediately generated. Subsequently, $SF_6$ gas is injected into section II through an inflow hole, while air is exhausted through an outflow hole. In this way, an $SF_6$ layer surrounded by air is created. Note that the thin filaments can prevent the soap film from shrinking and sliding into section II, and thus the shape of the layer can be maintained for a certain period of time. An oxygen concentration detector is placed at the outflow hole to monitor the oxygen concentration in the gas mixture exhausted from the layer. When the measured oxygen concentration meets the experimental requirement (below 2 %), the inflow and outflow holes are sealed immediately. Following this, a drawer containing sections I, II and III is inserted into the convergent test section. To minimise gas diffusion across the soap film, the insertion process is completed within one minute. This approach allows precise control over both the shape and thickness of the $SF_6$ layer, ensuring high repeatability of the experimental results.

In a cylindrical coordinate system, the outer and inner interfaces of the layer can be parametrised as $r_i = R_i + a_i \cos(n\theta + \varphi_i)$, where $i = 1$ ($i = 2$) refers to the outer (inner) interface, $R$ to the radius of the interface, $a$ to the perturbation amplitude, $\theta$ to the azimuthal angle, $n$ to the azimuthal mode number and $\varphi$ to the perturbation phase. The cylindrical convergent shock has a reproducible Mach number of $M_i = 1.27 \pm 0.01$ when it encounters the initial interface. A high-speed camera (NOVA S9, Photron Limited) combined with a schlieren system is used to record the flow field illuminated by a DC-stabilised light source (DCR III, SCHOTT North America, Inc.). The high-speed camera operates at a frame rate of 50 000 frames per second (f.p.s.) with a shutter time of 1 μs. The ambient pressure and temperature are 101.1 kPa and 298.0 K, respectively.

## 3. Experimental results and discussions

### 3.1. *Background flow*

The RM instability flow is a combination of two types of motion: the background motion, which causes the entire interface to move downwards, and the local rotational motion, which causes the interface amplitude to increase over time (Stanic *et al.* 2012; Dell *et al.* 2017; Zhang *et al.* 2023*c*). The former is determined by the shock intensity and fluid properties (e.g. density and specific heat ratio), which exists in both perturbed and unperturbed cases. The latter quantifies the degree of instability, which occurs only in the case of a perturbed interface. In most circumstances, such as planar RM instability, the former is uniform and does not influence the latter, allowing the two motions to be decoupled. However, for the convergent RM instability, the background flow is time-dependent, which induces RT stability or instability, significantly affecting the instability growth. Therefore, obtaining the background motion is crucial for fully understanding and predicting the convergent RM instability. Since there is currently no analytical solution for such a background flow, a quasi-one-dimensional (1-D) experiment corresponding to an



https://doi.org/10.1017/jfm.2025.178 Published online by Cambridge University Press

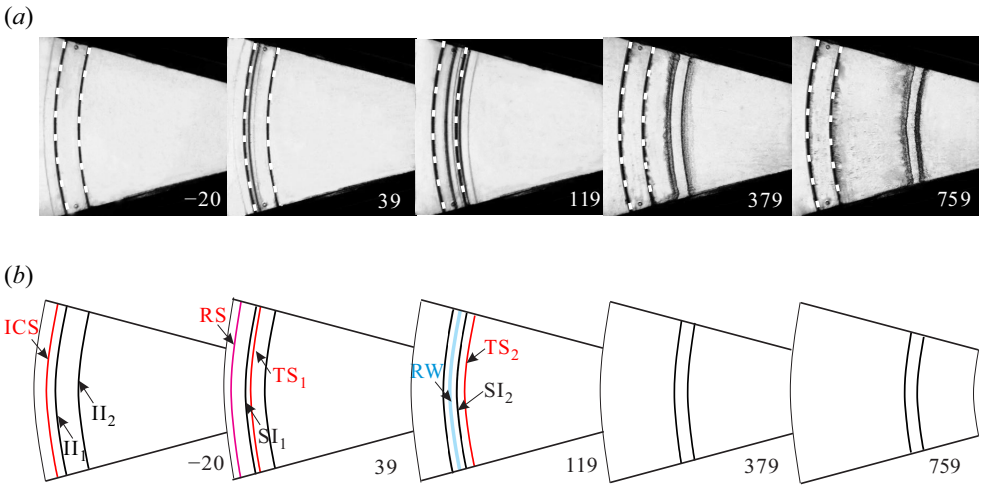



Figure 2. (*a*) Schlieren images showing the evolution of an unperturbed $SF_6$ layer accelerated by a cylindrical convergent shock. (*b*) Sketches of the waves and interfaces at corresponding moments. The white dotted lines indicate the thin filaments used to form the initial interfaces. The unit of numbers is μs. ICS, the incident cylindrical shock; $II_i$, the initial interface ($i = 1, 2$ refers to the outer and inner interfaces, respectively); $SI_i$, the shocked interface; $TS_i$, the transmitted shock; RS, the reflected shock; RW, the rarefaction wave.

unperturbed cylindrical $SF_6$ layer surrounded by air subjected to a cylindrically convergent shock is first conducted.

Representative schlieren images illustrating the motions of the interfaces and waves for the unperturbed case are displayed in figure 2(*a*). To better illustrate the motion of the gas layer, sketches of the waves and interfaces at corresponding moments are provided in figure 2(*b*). The time origin in this work is defined as the moment at which the incident shock arrives at the mean position of the outer interface. At the beginning (-20 μs), both the outer ($II_1$) and inner ($II_2$) interfaces, along with the incident convergent shock (ICS), are clearly discerned. This demonstrates the feasibility and reliability of the current experimental methods. As time goes on, the ICS propagates downstream and impinges upon the outer air/$SF_6$ interface, bifurcating immediately into an ingoing transmitted shock ($TS_1$) and an outgoing reflected shock (RS) (39 μs). After that, the shocked outer interface starts moving and gradually leaves its original position. Later, the $TS_1$ collides with the inner interface, splitting into a second transmitted shock ($TS_2$) and an outgoing rarefaction wave (RW) (119 μs). The shocked inner interface moves downstream following the $TS_2$. Later, the outgoing RW stretches and accelerates the outer interface, while simultaneously generating an ingoing compression wave within the layer (not visible in schlieren images due to its weak intensity). As expected, no reflected shock is observed here since the convergent shock tube has an open outlet. The white dotted lines in figure 2(*a*) indicate the locations of the protruding filaments (i.e. the locations of initial interfaces). It should be noted that the shock impact can cause the soap film to atomise into small droplets. According to Cohen (1991) and Ranjan *et al.* (2008), the mean radius of soap droplets in the present experiment is estimated to be approximately 30 μm for $M \sim 1.3$. These droplets are negligibly small compared with the characteristic length scales of the flow and thus have a negligible influence on interface dynamics. This conclusion has been thoroughly validated in our previous work. For instance, previous numerical simulations of shock–bubble interactions that excluded soap droplets showed excellent agreement with experimental results in terms of both interface morphology and growth rate (Ding *et al.*



https://doi.org/10.1017/jfm.2025.178 Published online by Cambridge University Press

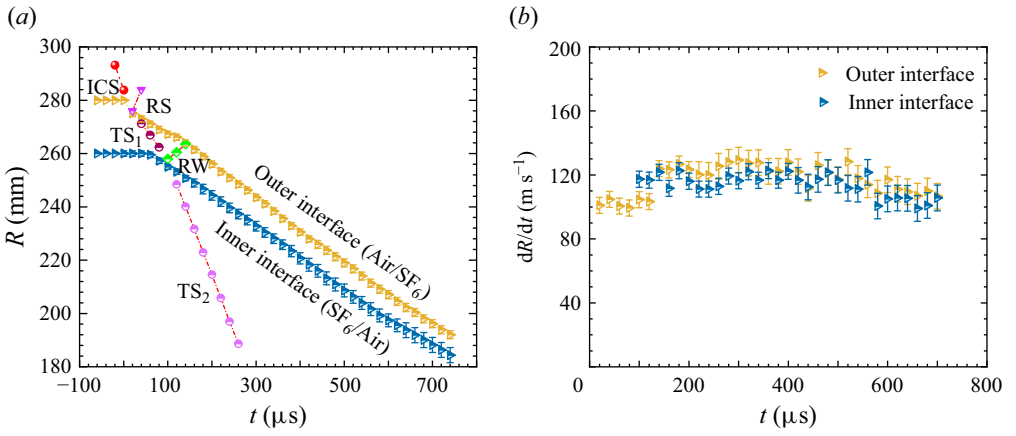



Figure 3. (*a*) Trajectories of the interfaces and waves. (*b*) Time derivatives of the interface displacement. The abbreviations are the same as those in figure 2.

2017*a*). Furthermore, shock-tube experiments on RM instability at single-mode interfaces, generated using the soap film technique, exhibited linear growth rates consistent with impulsive model predictions that ignore soap droplets (Liu *et al.* 2018). The consistency across experiments (with soap droplets), simulations and theories (without soap droplets) confirms that the influence of soap droplets on interface evolution is negligible. Also, the influence of boundary layer on the flow is negligible during the time of interest (Luo *et al.* 2019; Zhang *et al.* 2023*b*).

An $R-t$ diagram depicting the trajectories of the waves and interfaces is plotted in figure 3(*a*), which reflects the time-dependence of the flow field. The time derivative of the interface displacement is also given in figure 3(*b*). Slight fluctuations are observed in the calculated interface velocity, which is primarily due to the limited temporal resolution of the schlieren images. Accelerated by the incident convergent shock, the outer interface attains an initial velocity of 101.1 m s$^{-1}$. Subsequently, it is accelerated to 124.0 m s$^{-1}$ by the RW. After the impact of the first transmitted shock $TS_1$, the inner interface moves inwards at a velocity of 117.7 m s$^{-1}$. As the waves move away, both the inner and outer interfaces present uniform motion, with only slight deceleration at the later stage. It indicates that the RT effect is significantly mitigated in the current shock tube. Considering the measurement error, both interfaces can be regarded as moving uniformly throughout the entire experimental duration. The extended period of uniform motion for the inner and outer interfaces provides a rare opportunity to analyse the effects of nonlinearity and interface coupling on convergent RM instability, which will be discussed in § 3.2. Despite this, we emphasise that the base flow in our configuration is complex, characterised by a non-uniform pressure field behind the incident shock and an expansion-shock structure resulting from shock–interface interactions. This generates a spatially and temporally varying pressure field, which serves as the background flow for perturbation growth. Such a background flow is particularly crucial as it can significantly influence instability development through several mechanisms. First, the non-uniform pressure field behind the incident shock directly modulates baroclinic vorticity generation, the primary driving mechanism of the RM instability. Second, the expansion-shock structure introduces additional wave–interface interactions, altering perturbation growth rates through multiple reflection and transmission events. Third, the time-dependent nature of the flow field introduces additional effects that are absent in conventional planar configurations. These



https://doi.org/10.1017/jfm.2025.178 Published online by Cambridge University Press

characteristics of the base flow are essential for understanding interface dynamics and thus are carefully incorporated into the vortex method (§ 4).

Although a gas concentration detector is used to measure the oxygen concentration in the gas mixture exhausted from the outflow hole, it ensures only a high concentration of $SF_6$ inside the layer rather than directly measuring the mass fraction of $SF_6$. In this work, the mass fraction of $SF_6$ is estimated using the following method. In a 1-D flow where a shock impacts a light/heavy interface, the resulting flow typically consists of four uniform regions separated by a reflected shock, a transmitted shock and the interface itself. When a cylindrical convergent shock has just passed across an unperturbed cylindrical interface, the flow can be approximated as 1-D along the radial direction. According to 1-D gas dynamics theory, we can establish relations between the flow parameters on either side of the reflected and transmitted shocks. Also, a compatibility relation exists (i.e. continuity of normal velocity and pressure) across the interface. With these relations, the following equation can be derived:

$$\left[\frac{(\Lambda_2-1)\,\rho_1}{(\Lambda_1-1)\,\rho_2}\right]^{1/2}\frac{P_t-1}{(P_t\Lambda_2+1)^{1/2}}=\frac{P_i-1}{(P_i\Lambda_1+1)^{1/2}}-\left(\frac{\rho_1}{\rho_1'}\right)^{1/2}\frac{P_t-P_i}{(P_t\Lambda_1+P_i)^{1/2}},\quad(3.1)$$

where

$$\left.\begin{aligned}\Lambda_1&=(\zeta_1+1)/(\zeta_1-1)\\ \Lambda_2&=(\zeta_2+1)/(\zeta_2-1)\\ P_i&=1+2\zeta_1/(\zeta_1+1)\left(M_i^2-1\right)\\ \rho_1/\rho_1'&=\left[(\zeta_1-1)\,M_i^2+2\right]/\left[(\zeta_1+1)\,M_i^2\right]\end{aligned}\right\}.\quad(3.2)$$

Here, $\zeta_1$ and $\rho_1$ are the specific heat ratio and density outside the layer, respectively, $\zeta_2$ and $\rho_2$ are the specific heat ratio and density inside the layer, respectively, $P_i$ ($P_t$) refers to the pressure ratio across the incident shock (transmitted shock) and $\rho_i'$ to the fluid density behind the incident shock. In experiment, the velocity of the incident shock propagating in pure air is measured to be 445.0 m s$^{-1}$, corresponding to $M_i = 1.27$. Based on the measured velocities of the incident and transmitted shocks, the mass fraction of $SF_6$ can be determined through an iterative method. Specifying an arbitrary initial value between 0 and 1 for the mass fraction of $SF_6$ inside the layer, the flow parameters inside the layer (e.g. $\rho_2$ and $\zeta_2$) can be obtained. Substituting these known parameters into (3.1), the pressure ratio across the transmitted shock ($P_t$) can be solved, namely, the strength of the transmitted shock is available. If the Mach number of the transmitted shock obtained is higher than the measured one, the value of mass fraction is slightly reduced; otherwise, it is increased. This process is repeated multiple times until the calculated value is in good agreement with the measured one (i.e. their difference is less than 0.1 %). For the unperturbed case here, the mass fraction of $SF_6$ is calculated to be 92.5 %. Using this value, the flow velocity behind the transmitted shock is calculated to be 99.2 m s$^{-1}$ based on 1-D gas dynamics theory. This result is in good agreement with the measured value (101.1 $\pm$ 2.0 m s$^{-1}$), indicating the reliability of the concentration calculation method.

### 3.2. *Evolution of perturbed layer*

Eight types of perturbed $SF_6$ layers with various thicknesses and shapes, subjected to a cylindrical convergent shock, are then examined. Specifically, two layer thicknesses are considered: the outer interface is fixed at $R_{1_0} = 280$ mm, while the inner interface takes radii of $R_{2_0} = 260$ mm and 240 mm, corresponding to the layer thicknesses of $d_0 = 20$ mm and 40 mm, respectively. For each thickness, various shapes of the inner and



https://doi.org/10.1017/jfm.2025.178 Published online by Cambridge University Press

| Case | $a_{1_0}$ | $a_{2_0}$ | $R_{1_0}$ | $R_{2_0}$ | $\Delta\varphi$ | $A$ | $V_{ics}$ | $V_{ts_1}$ | $\Delta V_1$ | $\Delta V_2$ |
|---|---|---|---|---|---|---|---|---|---|---|
| d20-US | 0 | 3 | 280 | 260 | — | 0.60 | 441.1 | 213.9 | 98.0 | 116.0 |
| d20-SU | 3 | 0 | 280 | 260 | — | 0.59 | 440.8 | 219.4 | 102.0 | 120.0 |
| d20-IP | 3 | 3 | 280 | 260 | 0 | 0.59 | 439.8 | 219.3 | 100.2 | 117.1 |
| d20-AP | 3 | 3 | 280 | 260 | $\pi$ | 0.59 | 440.8 | 219.4 | 99.7 | 117.7 |
| d40-US | 0 | 3 | 280 | 240 | — | 0.60 | 440.8 | 213.7 | 98.2 | 115.1 |
| d40-SU | 3 | 0 | 280 | 240 | — | 0.59 | 440.8 | 219.4 | 99.7 | 117.8 |
| d40-IP | 3 | 3 | 280 | 240 | 0 | 0.59 | 438.8 | 212.8 | 98.9 | 114.7 |
| d40-AP | 3 | 3 | 280 | 240 | $\pi$ | 0.58 | 438.8 | 221.8 | 100.4 | 118.7 |

Table 1. Detailed parameters corresponding to initial conditions for each case. $R_{1_0}$ ($R_{2_0}$) is the initial radius of the outer (inner) interface; $a_{1_0}$ ($a_{2_0}$) is the initial amplitude of the outer (inner) interface; $\Delta\varphi$ is the phase difference between the initial perturbations at the outer and inner interfaces; $A = (\rho_2 - \rho_1)/(\rho_2 + \rho_1)$ is the Atwood number; $V_{ics}$ is the velocity of the incident cylindrical shock; $V_{ts_1}$ is the velocity of the transmitted shock; $\Delta V_1$ ($\Delta V_2$) is the post-shock velocity of the outer (inner) interface. The radius and amplitude are in mm and the velocity is in m s$^{-1}$.

outer interfaces are considered: unperturbed outer interface and sinusoidal inner interface (case US); sinusoidal outer interface and unperturbed inner interface (case SU); sinusoidal outer and inner interfaces with in-phase perturbations (case IP); and sinusoidal outer and inner interfaces with anti-phase perturbations (case AP). For ease of reference, we designate a gas layer as case d20/d40-SU/US/IP/AP, where the first symbol represents the layer thickness and the second denotes the layer shape. For example, case d20-SU refers to a 20 mm thick layer with a sinusoidal outer interface and an unperturbed inner interface. In this work, interface perturbations with an azimuthal mode number of $n = 24$ and an initial amplitude of $a = 3$ mm are adopted. These parameters are carefully chosen to enable clear observation of both linear and nonlinear growth stages within our experimental window while maintaining high measurement precision. Specifically, the selection of these parameters is based on several considerations. First, the mode number $n = 24$ ensures the observation of multiple wavelengths within our field of view, which is essential for obtaining statistically reliable amplitude measurements. Second, the initial amplitude $a = 3$ mm is chosen to be sufficiently small relative to the wavelength to allow observation of the linear stage, yet large enough to ensure accurate measurements and to reach the nonlinear stage within the experimental time frame. While a systematic study of different initial amplitudes and frequencies would be valuable, it lies beyond the scope of the current work, which primarily focuses on elucidating the effects of interface coupling and reverberating waves on instability growth. Detailed parameters corresponding to the initial conditions for each case are listed in table 1, where the Atwood number is defined as $A = (\rho_2 - \rho_1)/(\rho_2 + \rho_1)$. The parameters, such as shock strength, gas concentration and interface positions, are nearly identical across these cases, indicating that the background flow remains consistent.

### 3.2.1. *Schlieren results*

Developments of the interface morphologies and wave patterns, illustrated by sequences of schlieren images, are presented in figure 4. Here, we take case d40-US as an example to detail the evolution process. At the beginning ($-18$ μs), an incident convergent shock ICS, along with an unperturbed outer interface $\mathrm{II}_1$ and a sinusoidal inner interface $\mathrm{II}_2$, is clearly observed. The velocity of the incident shock is measured to be 441.1 m s$^{-1}$ just before its collision with the outer interface, corresponding to Mach number $M_i = 1.27$.



https://doi.org/10.1017/jfm.2025.178 Published online by Cambridge University Press

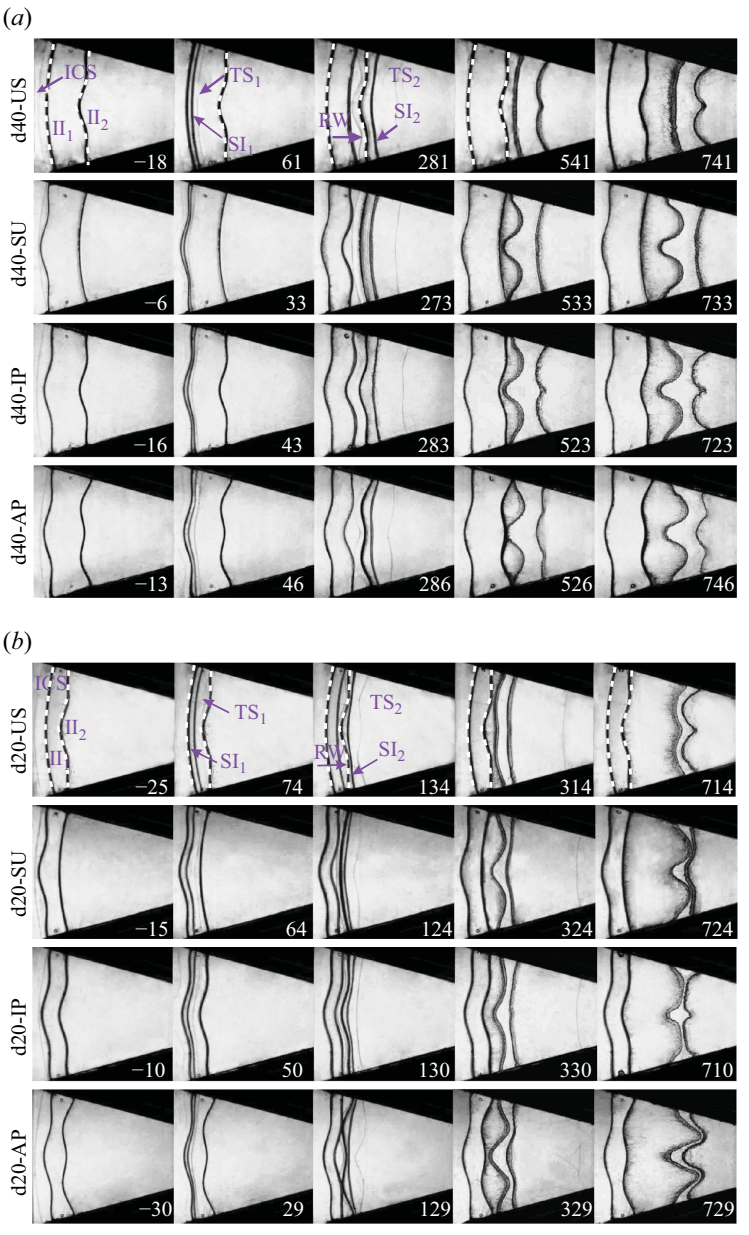



Figure 4. Schlieren images showing the developments of wave patterns and interfacial morphologies for all cases. The white dotted lines indicate the thin filaments used to form the soap film interfaces. The symbols are the same as those in figure 2. The unit of numbers is μs.

After the incident shock passes across the outer interface, it bifurcates into an upstream-moving reflected shock RS and a downstream-moving transmitted shock $TS_1$. The shocked outer interface $SI_1$ moves downstream with an initial velocity of approximately 98.2 m s$^{-1}$. During this process, it maintains a perfectly cylindrical shape with no instability due to the complete alignment between the incident shock and the initial interface. Afterwards, the cylindrical transmitted shock $TS_1$ collides with the sinusoidal inner interface, immediately bifurcating into a second transmitted shock $TS_2$ and an outgoing rarefaction wave RW (281



https://doi.org/10.1017/jfm.2025.178 Published online by Cambridge University Press

μs). Differing from the unperturbed case, both the $TS_2$ and RW here exhibit a sine-like perturbation. Particularly, the RW has the same perturbation phase as the sinusoidal inner interface, while $TS_2$ presents an opposite phase. After the impact of $TS_1$, the amplitude of the inner interface experiences a sudden drop due to shock compression, then reduces gradually to zero (i.e. phase inversion) and finally increases persistently with an opposite phase. Despite the rapid deformation of the inner interface, the outer interface presents no instability during the entire experimental period (741 μs). This phenomenon is also seen in case d40-SU, where the outer interface exhibits a large perturbation amplitude at 733 μs, while the inner interface remains perfectly cylindrical. Previous studies have shown that, at late stages when the waves move away from the gas layer, the compressibility effect becomes negligible and interface coupling dominates the instability growth (Mikaelian 1995, 2005; Liang & Luo 2021). The decoupling of the inner and outer interfaces observed here indicates that the interface coupling effect is sufficiently weak for 40 mm thick layers.

As the layer thickness is reduced to 20 mm (e.g. case d20-US), the outer interface also presents no instability growth at the early stage. Later, the disturbed RW stretches and accelerates the outer interface, seeding a slight perturbation on it. As time proceeds, this small perturbation grows continuously with time. At late stages (714 μs), the outer interface exhibits a considerably large perturbation that is in phase with the perturbed inner interface. Similarly, in case d20-SU, the initially unperturbed inner interface presents a large perturbation that is in phase with the perturbed outer interface (724 μs). The present results manifest that interface coupling plays a significant role in the evolution of 20 mm thick layers. For case d20-AP, after the shock impact, the amplitude of the inner interface first suffers a gradual reduction to zero (i.e. phase inversion), then increases persistently with the same phase as the outer interface. In contrast, in case d20-IP, the deformed inner interface exhibits an opposite phase relative to the outer interface at late stages. According to the analysis of Mikaelian (2005), for two sinusoidal interfaces that have the same phase (opposite phases), interface coupling promotes (suppresses) the perturbation growth at either interface. This reasonably explains why the perturbation growth at either interface in case d20-AP is much quicker than that in case d20-IP. The present experimental results demonstrate that the phase difference between the two interfaces determines the interface coupling effect and further affects the instability growth rate at each interface. To more clearly reveal the effect of phase difference between the two interfaces on the layer evolution, contours of waves and interfaces at typical moments for the 20 mm thick layers with various shapes are depicted in figure 5. It should be emphasised that this is the first long-term observation of convergent RM instability in a gas layer. Although the observed phenomena qualitatively align with the RM instability triggered by planar shocks (Liang & Luo 2021) or divergent shocks (Zhang *et al.* 2023*a*), the experimental data offer a rare opportunity to analyse the regimes of convergent RM instability.

### 3.2.2. *Growth of perturbation amplitude*

Under the incompressible, inviscid and irrotational flow assumption, Wang *et al.* (2015) has derived a weakly nonlinear model for the cylindrical RM instability at an isolated single-mode interface. A brief description of this model is given below. A velocity potential is first introduced for either fluid across the interface, which satisfies the Laplace equation. By applying the kinematic and dynamic boundary conditions (i.e. normal velocities of both fluids match and also pressure is continuous across the interface), three additional equations for the velocity potentials are derived. By expanding the perturbation displacement and velocity potentials into a power series, the first-, second- and third-order governing equations, each expressed as a second-order ordinary differential equation, can



https://doi.org/10.1017/jfm.2025.178 Published online by Cambridge University Press

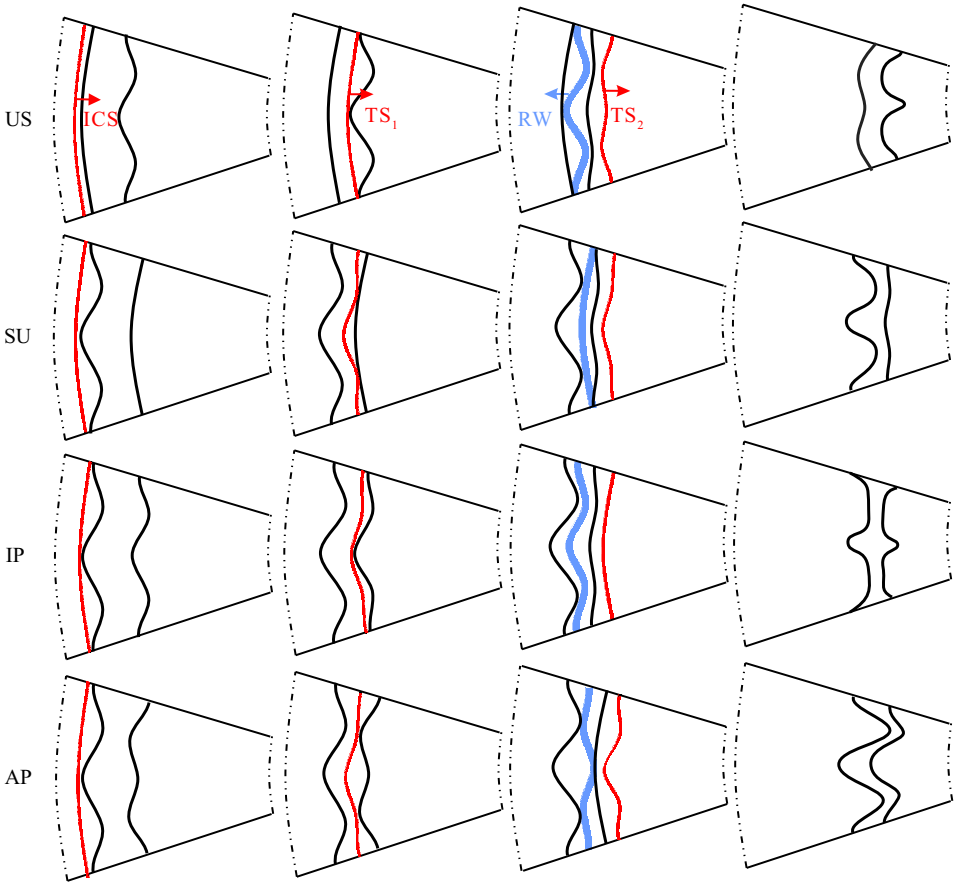



Figure 5. Sketches of the wave patterns and interface morphologies at typical moments for 20 mm thick layers. The symbols are the same as those in figure 2.

be obtained. It is important to note that obtaining a general solution for the perturbation growth at a cylindrical interface with an arbitrary implosion or explosion history is highly challenging. By assuming uniform motion of the interface, this problem becomes significantly simpler and a third-order analytical solution can be derived. For more details about the model, readers are referred to the original work (Wang *et al.* 2015).

Temporal variations of the amplitudes of the inner and outer interfaces for all perturbed layers are plotted in figure 6, with the predictions from Wang *et al.* (2015) provided for comparison. The amplitude is defined as half the total width of the interface, i.e. half the maximum distance between the spike head and the bubble tip. Note the parameters required by Wang *et al.* (2015), such as the initial growth rate, interface displacement, velocity and acceleration, are measured from experiment. We first discuss the instability growth at the outer interface. As seen in figures 6(*a*) and 6(*c*), for either thickness, the perturbation growths at the outer interface for the SU, IP and AP cases collapse quite well before the arrival of RW, which indicates a negligible interface coupling effect during the early stage. This can be interpreted from the perspective of pressure disturbances. In compressible fluids, perturbations at one interface propagate to another interface via pressure disturbances, which travel at the speed of sound. It means that these disturbances cannot cross through reverberating waves (such as RW) to influence the other interface.



https://doi.org/10.1017/jfm.2025.178 Published online by Cambridge University Press

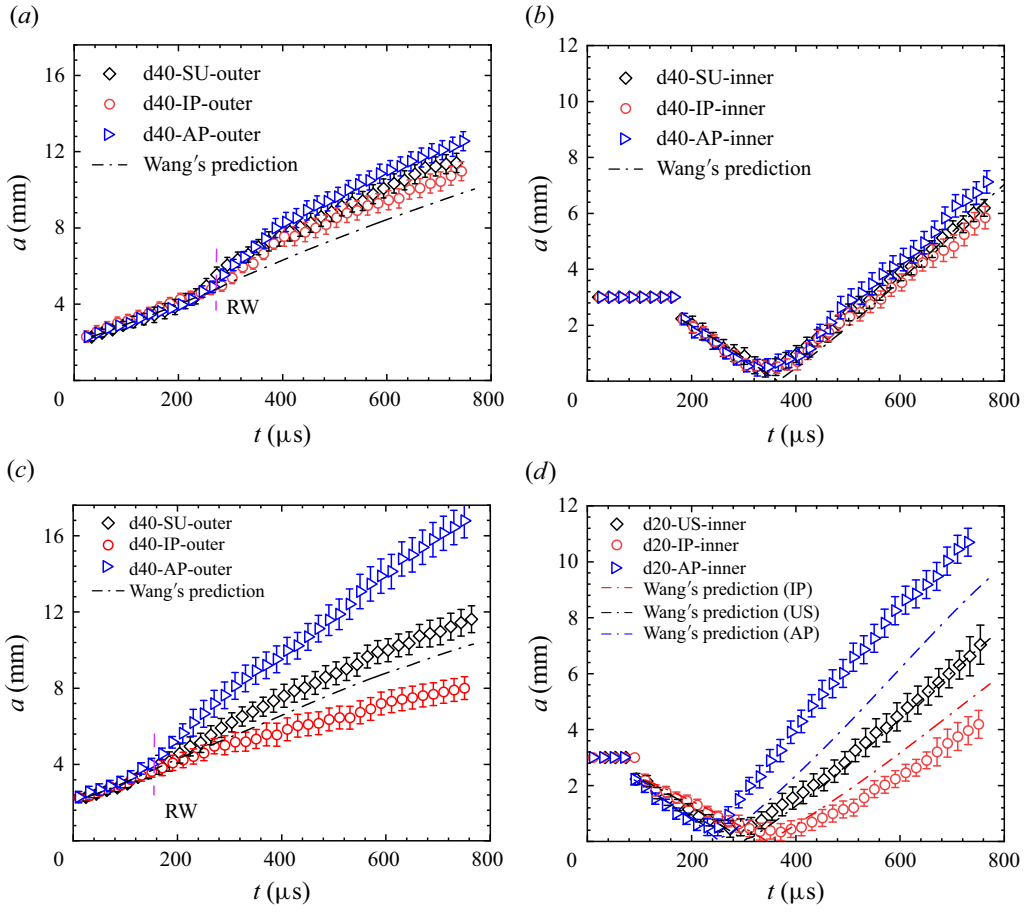



Figure 6. Comparison of the amplitude growths of the (*a*,*c*) outer and (*b*,*d*) inner interface between experiments and the prediction of Wang *et al.* (2015).

Thus, before the arrival of RW, the evolution of the outer interface suffers no influence of the inner interface and *vice versa*. This also explains why the weakly nonlinear model of Wang *et al.* (2015), developed for cylindrical RM instability at a single interface, provides a good prediction of instability growth before the arrival of RW for all cases. Later, the RW stretches and accelerates the outer interface, notably enhancing the instability growth except in case d20-IP (the reason is explained later). For a thick layer, the effect of RW is weakly dependent on the interface shape, as indicated by figure 6(*a*). It is seen that the RW significantly enhances the perturbation growth in case d40-AP, moderately in case d40-SU and minimally in case d40-IP. This can be explained by the wave patterns in figure 5, where the perturbed RW is out of phase with the deforming outer interface for the AP layer, producing more baroclinic vorticity, whereas it is in phase with the deforming outer interface for the IP layer, producing less baroclinic vorticity. Since the RW is weak in the present experiment, the difference in the instability growth among the three cases is small. At late stages, the amplitude of the outer interface remains consistent across all 40 mm thick layers, indicating a negligible interface coupling effect. This is confirmed by schlieren results, where the outer interface presents nearly the same perturbation at late stages across cases d40-AP, d40-IP and d40-SU.



https://doi.org/10.1017/jfm.2025.178 Published online by Cambridge University Press

For a thin layer, interface coupling becomes pronounced, and the instability growth is influenced by both the RW and interface coupling. For case d20-AP, the RW is out of phase with the outer interface (see figure 5), significantly enhancing the perturbation growth. Also, the interface coupling effect further promotes the instability growth in this case. As a result, this scenario exhibits the fastest instability growth following the RW impact. In case d20-IP, the RW is in phase with the outer interface, leading to only a modest increase in instability growth. Nevertheless, the interface coupling inhibits instability growth in this case. As a consequence, after the RW impact, the perturbation growth at the outer interface is slower compared with an isolated interface. It indicates that the influence of interface coupling outweighs the effect of RW. In case d20-SU, the effects of RW and interface coupling are moderate, resulting in a moderate growth rate that is slightly higher than that of an isolated interface. The present results show that both the effect of RW and interface coupling are highly sensitive to layer shape. Compared with the effect of RW, interface coupling plays a more significant role in instability growth, particularly at later stages.

Then, we examine the instability growth at the inner interface. As shown in figure 6(*b*), for thick layers, the instability growth at the inner interface remains consistent across the IP, AP and US cases. Given the initial growth rate measured from experiment, the model of Wang *et al.* (2015), which ignores the effect of rippled shock, gives a reasonable prediction of the instability growth throughout the entire experimental duration. This indicates that for thick layers, the effects of waves and interface coupling are negligibly weak, allowing the inner interface to evolve independently as if it were isolated. In contrast, for thin layers, notable discrepancy is observed among the IP, AP and US cases from the very beginning. Specifically, the AP case exhibits the largest initial growth rate (prior to phase inversion), the US case shows a moderate growth rate and the IP case has the smallest growth rate. This indicates that the effect of rippled $TS_1$ on the inner interface is significant and must be considered, which will be detailed in § 4. After phase inversion, the AP case continues to show the highest growth rate, the US case maintains a moderate rate and the IP case shows the smallest rate. This is attributed to the interface coupling effect: it significantly promotes instability growth in the d20-AP case, moderately promotes instability growth in the d20-SU case and suppresses instability growth in the d20-IP case. The model of Wang *et al.* (2015) fails to predict the perturbation growth at late stages, despite initially matching the experimental results. The discrepancy is primarily due to the neglect of interface coupling in the model of Wang *et al.* (2015). The underlying regimes driving the diverse perturbation growth behaviours observed here are explored in § 4.

## 4. Vortex method for convergent RM instability

The development of RM instability involves two distinct phases: the baroclinic vorticity production phase, which occurs as the shock wave passes through the interface, and the interface evolution phase, which occurs after the shock wave leaves the interface. Once the waves move away from the interface, the flow can be treated as incompressible. According to Kelvin's circulation theorem, vorticity cannot be produced within the fluid on either side of the interface in incompressible flows. It means that the baroclinic vorticity generated during the first phase must be confined to the interface at all times. From this perspective, the interface can be modelled as a vortex sheet. Thus, the instability growth at the interface can be determined by tracking the motion of the vortex sheet. This technique is commonly known as the vortex method. The detailed derivation of the original vortex method is provided in the Appendix. The vortex method has exhibited great potential for simulating the RT and KH instabilities (Baker *et al.* 1980, 1982; Tryggvason 1988; Sohn *et al.* 2010; Pfaff *et al.* 2012). However, it has seldom been applied to the RM instability.



https://doi.org/10.1017/jfm.2025.178 Published online by Cambridge University Press

Before applying this method to RM instability, two critical issues must be addressed. First, the original vortex method did not account for background flow, which is crucial in the case of RM instability. In particular, for convergent RM instability, an unsteady, non-uniform background flow exists, significantly affecting vortex sheet transport. Second, accurately estimating the vortex sheet strength along the initial interface immediately after shock passage poses a challenge. This problem involves compressible, multi-component flow and is notably more complex than the RT and KH instabilities (Sohn *et al.* 2010; Sohn 2011).

In this section, a new equation for the transport of vortex sheet strength that accounts for the influence of the background flow is first derived. Then, the calculation of vortex sheet strength along the initial interface for general convergent RM instability (i.e. a disturbed cylindrical shock interacts with a perturbed cylindrical interface) is provided based on our recent analysis (Li *et al.* 2022). By numerically solving the new transport equation of the vortex sheet, along with its motion equation, an extended vortex method for the convergent RM instability is developed.

### 4.1. *Considering the background flow*

In contrast to the RT and KH instabilities, in the context of RM instability, each fluid element at the interface not only experiences local rotational motion, but also acquires a background velocity due to the shock impact. Especially, the convergent RM instability involves an unsteady, non-uniform background flow, which could significantly influence the transport of vortex sheet strength. Therefore, accurately estimating the effect of background flow on the vortex sheet transport is crucial for the vortex method. For this purpose, the velocity on either side of the interface is decomposed into two components:

$$\boldsymbol{u}_i = \boldsymbol{u}_i' + \boldsymbol{u}_\infty, \tag{4.1}$$

where $\boldsymbol{u}_i'$ is the shear velocity, which is discontinuous across the interface, and $\boldsymbol{u}_\infty$ is the background velocity, which remains invariant across the interface. Thus, the vortex sheet strength can be expressed as

$$\gamma = (\boldsymbol{u}_1 - \boldsymbol{u}_2)\cdot\boldsymbol{s} = (\boldsymbol{u}_1' - \boldsymbol{u}_2')\cdot\boldsymbol{s}. \tag{4.2}$$

Also, the Lagrange velocity of the interface can be written as

$$\boldsymbol{U} = (\boldsymbol{u}_1 + \boldsymbol{u}_2)/2 = \boldsymbol{U}' + \boldsymbol{u}_\infty, \tag{4.3}$$

where $\boldsymbol{U}' = (\boldsymbol{u}_1' + \boldsymbol{u}_2')/2$ denotes the average of the shear velocities on either side of the interface. Substituting (4.2) and (4.3) into the governing equation of the original vortex method (A6), an extended transport equation for the vortex sheet strength accounting for the background flow is obtained:

$$\begin{aligned}\frac{\mathrm{d}\gamma}{\mathrm{d}t} + \gamma\left(\frac{\partial \boldsymbol{U}'}{\partial s} + \frac{\partial \boldsymbol{u}_\infty}{\partial s}\right)\cdot\boldsymbol{s} = 2A\left[\left(\frac{\mathrm{d}\boldsymbol{U}'}{\mathrm{d}t} + \frac{\mathrm{d}\boldsymbol{u}_\infty}{dt}\right)\cdot\boldsymbol{s} + \frac{1}{8}\frac{\partial \gamma^2}{\partial s}\right] + 2A\boldsymbol{g}\cdot\boldsymbol{s} \\ - \frac{2}{\rho_1+\rho_2}\frac{\partial\,(p_1 - p_2)}{\partial s},\end{aligned} \tag{4.4}$$

where

$$\frac{d\boldsymbol{U}'}{dt} = \frac{\partial \boldsymbol{U}'}{\partial t} + \left(\boldsymbol{U}' + \boldsymbol{u}_\infty\right)\cdot\nabla\boldsymbol{U}'; \qquad \frac{d\boldsymbol{u}_\infty}{dt} = \frac{\partial \boldsymbol{u}_\infty}{\partial t} + \left(\boldsymbol{U}' + \boldsymbol{u}_\infty\right)\cdot\nabla\boldsymbol{u}_\infty. \tag{4.5}$$

Equation (4.4) is referred to as the vortex-b model in this work.



https://doi.org/10.1017/jfm.2025.178 Published online by Cambridge University Press

The term $\partial \boldsymbol{u}_\infty/\partial s$ on the left-hand side of (4.4) represents the stretching of the vortex sheet caused by non-uniform background flow. The term $\mathrm{d}\boldsymbol{u}_\infty/\mathrm{d}t$ on the right-hand side of (4.4) represents the generation/elimination of vorticity caused by unsteady background flow. In the context of RT and KH instabilities, the background velocity is typically zero, i.e. $\boldsymbol{u}_\infty = 0$. For this situation, (4.4) reduces to the original vortex sheet model represented by (A6). For the planar RM instability, the background velocity is constant (i.e. $\mathrm{d}\boldsymbol{u}_\infty/\mathrm{d}t = 0$ and $\partial \boldsymbol{u}_\infty/\partial s = 0$), and (4.4) also reduces to (A6). It indicates that the background flow in planar RM instability produces no effect on the vortex transport and can be ignored. However, for the convergent RM instability, the background velocity is unsteady in time ($\mathrm{d}\boldsymbol{u}_\infty/\mathrm{d}t \neq 0$) and also non-uniform in space ($\partial \boldsymbol{u}_\infty/\partial s \neq 0$), significantly affecting the transport of vortex sheet strength. This is a unique characteristic of convergent RM instability, as has been demonstrated in experiment (Ding *et al.* 2017*b*). Considering there is no analytical solution for the background flow of convergent RM instability, in this work, $\boldsymbol{u}_\infty$ is obtained by fitting the interface position measured from experiment. Note in the present experiments, the surface tension of the soap film interface is negligibly small and also the effect of gravitational acceleration on the interface evolution is negligible. Thus, the last two terms on the right-hand side of (4.4) can be ignored.

Given the position and strength of a vortex sheet, the shear-induced velocity of any fluid point at the vortex sheet, $\boldsymbol{U}'$, can be calculated according to the Birkhoff–Rott equation:

$$u - i\,v = \frac{i}{2\lambda}\int_0^\lambda \gamma' \cot\frac{\pi(z - z')}{\lambda}\mathrm{d}s'. \tag{4.6}$$

Here, $u$ and $v$ represent the horizontal and vertical components of the shear-induced velocity $\boldsymbol{U}'$, $\lambda$ is the wavelength, $z = x + \mathrm{i}y$ in complex notation, and $\gamma' = \gamma(s')$, $z = z(s)$, $z' = z(s')$.

As we know, either the KH, RT or RM instability could develop into a roll-up at the late nonlinear stage, which corresponds to the formation of singularities in the vortex method. To avoid the formation of singularities, a desingularisation parameter, $\delta$, originally proposed by Krasny (1986), is applied to (4.6). Then, the velocity of each fluid point at the vortex sheet is calculated by

$$\begin{aligned} u &= \frac{1}{2\lambda}\int_0^\lambda \frac{\sinh(ky - ky')}{\cosh(ky - ky') - \cos(kx - kx') + \delta^2}\gamma' ds', \\ v &= -\frac{1}{2\lambda}\int_0^\lambda \frac{\sin(kx - kx')}{\cosh(ky - ky') - \cos(kx - kx') + \delta^2}\gamma' \mathrm{d}s'. \end{aligned} \tag{4.7}$$

In this work, $\delta = 0.01$ is adopted. The interface position is governed by

$$\mathrm{d}z/\mathrm{d}t = \boldsymbol{U}' + \boldsymbol{u}_\infty. \tag{4.8}$$

Given the initial distribution of vortex sheet strength, temporal evolution of the vortex sheet can be obtained by numerically solving (4.4), (4.7) and (4.8). During this process, the vortex sheet is usually discretised into several hundred to a thousand Lagrangian points. Time integration is performed using an iteration method following Sohn *et al.* (2010). A convergence study indicates that $\Delta t = 0.5\ \mu\mathrm{s}$ provides sufficient accuracy for our results and is therefore selected as the time step for all calculations in this work.

### 4.2. *Estimating the initial vortex sheet strength*

For the RT and KH instabilities, the initial vortex sheet strength can be readily specified (Sohn *et al.* 2010; Sohn 2011). In contrast, for the RM instability, the initial vortex sheet strength is influenced by the dynamic interaction between the incident shock and



https://doi.org/10.1017/jfm.2025.178 Published online by Cambridge University Press

the material interface. This interaction in compressible flow complicates the estimation of vortex sheet strength significantly. For a planar shock interacting with a perturbed interface, a scaling law that clearly reveals the vortex sheet strength along the interface has been derived based on shock dynamics theory (Samtaney & Zabusky 1994; Samtaney *et al.* 1998). It is formulated as

$$\gamma(s) = \frac{\mathrm{d}\Gamma}{\mathrm{d}s} = \frac{2c_0}{\zeta+1}\left(1-\frac{1}{\sqrt{\eta}}\right)\left(1+M^{-1}+2M^{-2}\right)(M-1)\sin\alpha \tag{4.9}$$

for a light/heavy interface, and

$$\gamma(s) = \frac{\mathrm{d}\Gamma}{\mathrm{d}s} = \frac{4c_0}{\zeta+1}\left(1-\frac{1}{\sqrt{\eta}}\right)\frac{M^2-1}{1+\frac{2\zeta}{\zeta+1}\left(M^2-1\right)}\sin\alpha \tag{4.10}$$

for a heavy/light interface. Here, $M$ is the shock Mach number, $\eta$ the density ratio across the interface, $c_0$ the sound speed of the pre-shock fluid, $\zeta$ the specific heat ratio of the gas, and $\alpha$ the angle between the shock and interface. The above equations account for the variation in the angle between the shock and the interface during the dynamic process of shock–interface interaction. In convergent RM instability, in addition to the variation in the angle between the shock and interface, the shock strength also varies continuously during the shock–interface interaction process. Moreover, for the convergent RM instability at a perturbed gas layer, the inner interface may be impacted by a distorted transmitted shock, for which the shock strength is non-uniform along its surface. Estimating the initial vorticity distribution along an interface impacted by such a distorted convergent shock is challenging.

In this work, we consider a general convergent RM instability, i.e. a sinusoidally distorted shock interacts with a single-mode interface in cylindrical geometry. Considering that the shock–interface interaction occurs within a very short period of time, the shock Mach number is assumed to remain constant during this process. With this assumption, the vortex sheet strength at the fluid point $(r,\theta)$ on the interface can be calculated as

$$\gamma(\theta) = \frac{\mathrm{d}\Gamma}{\mathrm{d}\theta}(\theta) = \frac{2c_0}{\zeta+1}\left(1-\frac{1}{\sqrt{\eta}}\right)\left(1+M^{-1}(\theta)\right)+2M^{-2}(\theta)(M(\theta)-1)\sin\alpha_1(\theta) \tag{4.11}$$

for a fast/slow interface, and

$$\gamma(\theta) = \frac{\mathrm{d}\Gamma}{\mathrm{d}\theta}(\theta) = \frac{4c_0}{\zeta+1}\left(1-\frac{1}{\sqrt{\eta}}\right)\frac{M^2(\theta)-1}{1+\frac{2\zeta}{\zeta+1}\left(M^2(\theta)-1\right)}\sin\alpha_2(\theta) \tag{4.12}$$

for a slow/fast interface. Here,

$$\sin\alpha_i(\theta) = \frac{\left(a_{i_0}^{+}r_{s_i}-a_{s_i}r_i^{+}\right)n\sin(n\theta)}{\sqrt{{r_{s_i}}^2+\left(na_{s_i}\sin(n\theta)\right)^2}}. \tag{4.13}$$

Here, $r_{s_i}=R_{s_i}+a_{s_i}\cos(n\theta)$ is the shock position with $R_{s_i}$ being the average radius of shock and $a_{s_i}$ being the perturbation amplitude of the shock, $a_{i_0}^{+}$ is the initial amplitude of the shocked interface, and $r_i^{+}=R_i^{+}+a_{i_0}^{+}\cos(n\theta)$ is the initial radius of the shocked interface. For more details on the derivation process, readers are referred to the original work (Li *et al.* 2022). Note that the post-shock amplitude is adopted in the above equations due to shock compression.



https://doi.org/10.1017/jfm.2025.178 Published online by Cambridge University Press

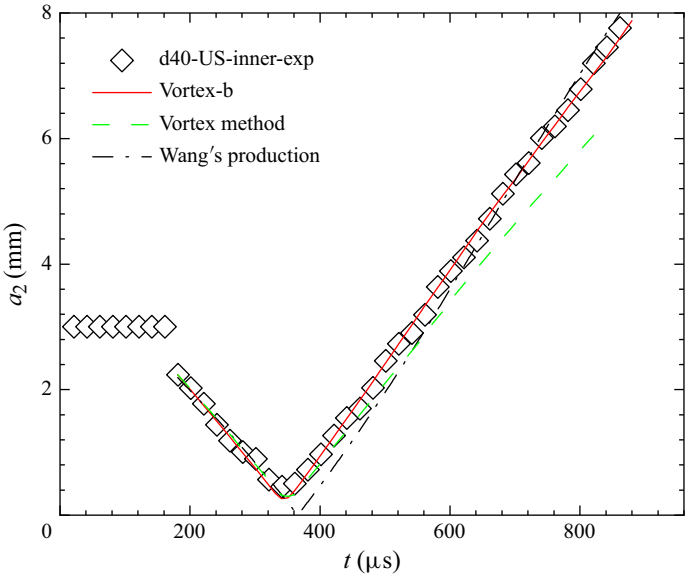



Figure 7. Comparison of the amplitude growth of the inner interface for case d40-US among the experiment, the prediction of Wang *et al.* (2015), the original vortex method and the vortex-b method.

Comparison of the instability growth at an isolated single-mode interface among the experiment, the prediction of Wang *et al.* (2015) and the current vortex method is shown in figure 7. It is found in § 3.2 that for thick layers ($d = 40$ mm), the evolutions of the inner and outer interfaces are nearly decoupled. Thus, the perturbation growth at the inner interface in case d40-US can represent the RM instability at an isolated single-mode interface. This is confirmed by the good agreement between the experimental data and the prediction of Wang *et al.* (2015). The vortex-b model, which incorporates the background flow, provides a more accurate prediction of the instability growth than the original vortex model. This demonstrates the significant role of the background flow in the development of convergent RM instability.

The vortex-b model fails to predict the convergent RM instability in other gas layers (e.g. case d20-AP, see figure 10.) This failure arises because the convergent RM instability introduces noticeable waves reverberating within the layer, which significantly influences the instability growth at each interface, as illustrated in figures 5 and 6. Furthermore, in thin layers, interface coupling becomes more pronounced, further affecting the instability growth at both interfaces. These effects are not considered in the current vortex-b method. Our subsequent analysis will address these factors.

### 4.3. *Involving the effect of reverberating waves*

We first consider the effect of the rippled $TS_1$ on the evolution of the inner interface. It is important to emphasise that the interaction between the rippled $TS_1$ and the perturbed inner interface belongs to non-standard RM instability (Ishizaki *et al.* 1996; Zou *et al.* 2019). This type of instability involves more complex regimes compared with the standard RM instability (i.e. a uniform shock impacts a perturbed interface). According to previous studies (Ishizaki *et al.* 1996; Zhang *et al.* 2018*b*), a rippled shock can initiate instability growth through two mechanisms: baroclinic vorticity, which arises from the misalignment between pressure and density gradients at the interface, and velocity perturbation, which results from the non-uniform Mach number along the shock surface.



https://doi.org/10.1017/jfm.2025.178 Published online by Cambridge University Press

| Case | $M_2$ | $a^+_{2_0}$ | $a_s$ | $\dot{a}_{2_0}$ | $\dot{a}_s(t_{ts})$ | $v_s$ | $\zeta_2$ | $c_2$ |
|---|---|---|---|---|---|---|---|---|
| d40-US | 1.40 | 2.23 | 0.00 | −10.0 | 0.0 | 0.0 | 1.11 | 153.9 |
| d40-SU | 1.40 | 0.20 | 0.15 | 1.1 | −2.4 | −1.3 | 1.12 | 158.4 |
| d40-IP | 1.41 | 2.21 | 0.14 | −10.5 | −2.3 | −1.2 | 1.12 | 157.3 |
| d40-AP | 1.40 | 2.22 | 0.14 | 10.2 | −2.5 | −1.3 | 1.12 | 159.2 |
| d20-US | 1.39 | 2.23 | 0.0 | −9.8 | 0.0 | 0.0 | 1.11 | 152.8 |
| d20-SU | 1.39 | 0.71 | 0.85 | 1.5 | −7.0 | −3.8 | 1.12 | 158.3 |
| d20-IP | 1.39 | 2.20 | 0.86 | −8.5 | −7.9 | −4.2 | 1.12 | 158.6 |
| d20-AP | 1.39 | 2.22 | 0.85 | 11.2 | −7.5 | −4.0 | 1.12 | 158.4 |

Table 2. Detailed parameters for the interaction of the inner interface with the perturbed $TS_1$. $M_2$ is the average Mach number of the perturbed $TS_1$ when it collides with the inner interface; $a^+_{2_0}$ is the post-shock amplitude of the inner interface; $a_s$ is the amplitude of the perturbed $TS_1$; $\dot{a}_{2_0}$ is the initial growth rate of the inner interface immediately after the impact of $TS_1$ (measured from experiment); $\dot{a}_s(t_{ts})$ is the growth rate of the amplitude of rippled $TS_1$; $v_s$ is the average growth rate induced by velocity perturbation; $\zeta_2$ is the specific heat ratio of the $SF_6$ layer; $c_2$ is the sound speed of the $SF_6$ layer; the units are mm and $\mathrm{m\,s^{-1}}$ for the length and growth rate, respectively.

To account for the baroclinic vorticity regime, an initial vortex sheet generated immediately after the shock–interface interaction should be accurately calculated. Here, the initial vortex sheet strength at the inner interface, generated by the impact of the rippled $TS_1$, can be calculated using (4.12). Then, we consider the velocity perturbation regime. In the case of a rippled shock, the shock strength varies continuously along its surface (i.e. stronger at the crest and weaker at the trough), resulting in a non-uniform velocity jump of the interface caused by the shock impact. This differs from the case of an unperturbed shock, where the interface acquires a uniform velocity immediately after the shock passage. According to the analysis of Ishizaki *et al.* (1996), the velocity perturbation caused by a rippled shock can be estimated as

$$v_s(t_0) = \frac{\Delta V}{V_s}\dot{a}_s(t_0), \tag{4.14}$$

where $\Delta V$ is the velocity jump of the interface, $V_s$ is the average velocity of the shock and $\dot{a}_s(t_0)$ is the growth rate of the amplitude of the rippled shock just before its collision with the inner interface. The calculation results for all cases are listed in table 2. Note that the inner interface, which is of a heavy/light configuration, first undergoes phase inversion and then exhibits instability growth. In an anti-phase layer, $\dot{a}_s\dot{a}_2 < 0$, indicating that phase inversion is inhibited by the rippled $TS_1$. Conversely, in an in-phase layer, $\dot{a}_s\dot{a}_2 > 0$, meaning that the rippled $TS_1$ acceleration phase undergoes inversion. This effect is more pronounced in thin layers, while it is significantly weaker in thick layers, as indicated by table 2. The reason is given below. For thick layers ($d = 40$ mm), the amplitude of the rippled shock is very small when it arrives at the inner interface and can be approximated as a uniform cylindrical shock. In the case of a uniform shock, $\dot{a}_s = 0$ and $v_s = 0$, meaning that the velocity perturbation is absent. In contrast, for thin layers ($d = 20$ mm), the amplitude of the rippled $TS_1$ is evident when it arrives at the inner interface, producing considerably large velocity perturbation. This indicates that the layer thickness is crucial, as it not only governs the strength of the interface coupling effect but also influences the evolution of the distorted transmitted shock, which in turn affects the evolution of the inner interface.

To provide further theoretical insight, the oscillation frequency for the $TS_1$ in the current experiments is calculated. According to Calvo-Rivera *et al.* (2023) and Bates (2012), the



https://doi.org/10.1017/jfm.2025.178 Published online by Cambridge University Press

oscillation frequency for a corrugated-piston-driven planar shock is given by

$$\omega_s = k_s\sqrt{c_2^2 - u_2^{*2}}, \tag{4.15}$$

where $k_s = 2\pi/\lambda_s$ is the spatial wavenumber of the rippled shock, with $\lambda_s$ being the spatial wavelength. Here, $c_2$ and $u_2^*$ are the post-shock speed of sound and the velocity of shock movement relative to the compressed gas, respectively. For a convergent, sinusoidally distorted shock, there is $\lambda_s = 2\pi R_{s_i}/n$. Based on this formula, the oscillation frequency of a perturbed converging shock increases as the radius decreases. This arises from the inability to associate the shock dynamics with a single characteristic length in the length-free problem. For instance, Huete *et al.* (2021) and Calvo-Rivera *et al.* (2022) discussed expanding shocks, where shock oscillation frequency decreases due to geometric divergence. Here, the oscillation period of $TS_1$ is calculated by $T_s = 2\pi/\omega_s$. For case d40-SU, $T_s$ is approximately 710 μs at $R_{s_i} = 280$ mm (outer interface) and 636 μs at $R_{s_i} = 240$ mm (inner interface). The time interval for $TS_1$ to propagate between these interfaces is $\Delta T \approx 165$ μs, which is approximately a quarter of the first oscillation period. It suggests that the amplitude of $TS_1$ approaches zero when it reaches the inner interface. This result aligns with the experimental schlieren images in figure 4, where the inner interface in case d40-SU remains perfectly cylindrical after interaction with $TS_1$. As shown in figure 6(*b*), the instability growth at the inner interface remains consistent for other thick layer cases (d40-US, d40-IP and d40-AP), suggesting that the amplitude of $TS_1$ is effectively zero at the inner interface in these cases. For case d20-SU, $T_s$ is approximately 693 μs at $R_{s_i} = 280$ mm (outer interface) and 655 μs at $R_{s_i} = 260$ mm (inner interface). The time interval $\Delta T \approx 85$ μs is less than a quarter of the first oscillation period, illustrating a visible perturbation at $TS_1$ prior to its interaction with the inner interface.

Considering the effect of the rippled $TS_1$, the radial component of the velocity of the inner interface can be expressed as

$$u_\infty^m = v_c(t) + v_s\cos(n\theta), \tag{4.16}$$

where $v_c(t)$ is the time-dependent radial velocity component of the entire interface induced by the shock. In this work, $v_c(t)$ is calculated using the first time-derivative of the interface position measured from experiment and $v_s$ is calculated using (4.14). Note that in cylindrical geometry, the velocity vector at each position on the interface directs to the geometric centre, namely its direction varies with $\theta$. Thus, the velocity vector can be expressed as

$$\boldsymbol{u}_\infty^m(\theta, t) = \boldsymbol{v}_c(\theta, t) + \boldsymbol{v}_s(\theta, t)\cos(n\theta). \tag{4.17}$$

By incorporating the above equation into (4.4), a new vortex method that accounts for the effect of $TS_1$ is obtained, which is referred to as the vortex-b-m method.

Next, we examine the influence of the rippled RW on the outer interface. A recent study (Zhang *et al.* 2023*a*) demonstrated that a rarefaction wave affects instability growth in two primary ways: it stretches the interface, thereby directly amplifying its amplitude, and it accelerates the background flow, producing RT stability or instability that suppresses or enhances the instability growth. First, we consider the stretching effect. Assuming the RW stretches the outer interface evenly, an empirical formula for the perturbation growth rate ($\boldsymbol{v}_{rw}$) caused by wave stretching was derived by Zhang *et al.* (2023*b*). It is formulated as

$$v_{rw} = \begin{cases} \dfrac{\Delta a_2^{rw}}{\Delta t_{rw}} = \dfrac{\Delta t_s\left(\Delta V_1^* - \Delta V_1\right)/2}{|\Delta t_s| + \Delta t_g} & (t_{rw} < t < t_{rw} + \Delta t_{rw}) \\ 0 & (\text{others}) \end{cases}, \tag{4.18}$$



https://doi.org/10.1017/jfm.2025.178 Published online by Cambridge University Press

| Case | $M_1$ | $a^+_{1_0}$ | $a_{(t=t_{rw})}$ | $a_{rw}$ | $\Delta t_{rw}$ | $\dot{a}_{1_0}$ | $v_{rw}$ |
|---|---|---|---|---|---|---|---|
| d20-US | 1.27 | 0.00 | 0.0 | 3.6 | 59.5 | 0.0 | −9.0 |
| d20-SU | 1.27 | 2.28 | 3.9 | −0.2 | 61.6 | 9.8 | 10.2 |
| d20-IP | 1.26 | 2.27 | 4.0 | 3.3 | 21.3 | 9.9 | 2.8 |
| d20-AP | 1.27 | 2.29 | 3.8 | −3.9 | 109.2 | 9.8 | 11.3 |
| d40-US | 1.27 | 0.00 | 0.0 | 3.6 | 70.6 | 0.0 | −10.8 |
| d40-SU | 1.27 | 2.28 | 4.9 | −0.1 | 87.6 | 9.7 | 10.9 |
| d40-IP | 1.26 | 2.30 | 5.1 | 3.5 | 40.7 | 9.9 | 5.7 |
| D40-AP | 1.26 | 2.29 | 4.7 | −3.7 | 130.3 | 9.7 | 11.2 |

Table 3. Detailed parameters for the interactions of the outer interface with the ICS and RW. $M_1$ is the Mach number of ICS; $a^+_{1_0}$ is the interface amplitude shortly after the passage of ICS (obtained from experiment); $a_{(t=t_{rw})}$ is the amplitude of the outer interface at the time $t_{rw}$; $a_{rw}$ is the amplitude of the RW; $\Delta t_{rw}$ is the time duration for RW passing through the outer interface; $\dot{a}_{1_0}$ is the initial growth rate of the outer interface after the impact of ICS; $v_{rw}$ is the average growth rate of the outer interface induced by RW; the units are μs, mm and m s$^{-1}$ for the time, length and growth rate, respectively.

where $t_{rw}$ is the time when the RW encounters the interface, $\Delta t_{rw}$ is the time duration for the RW passing through the interface, $\Delta a_2^{rw}$ is the amplitude increment caused by the stretching effect, $\Delta V_1^*$ is the average velocity of the interface impacted by the RW, and $\Delta t_s$ is the time duration between the moments when the crest and trough of the leading front of RW encounter the interface. The calculation results for all cases are listed in table 3.

Then, we examine the effect of interface acceleration caused by RW. This is achieved by incorporating the time-dependent interface velocity, $\boldsymbol{v}_c(\theta, t)$, which is approximated by the first time-derivative of the interface trajectory measured from experiment, into the background velocity. Considering both the acceleration and stretching effects caused by RW, the background velocity is changed to

$$\boldsymbol{u}^m_\infty(\theta, t) = \boldsymbol{v}_c(\theta, t) + \boldsymbol{v_{rw}}(\theta, t)\cos(n\theta). \tag{4.19}$$

Incorporating the above equation into (4.4), a new vortex method that considers the effect of RW is obtained. In this work, the vortex method, in which the background velocity involves the effects of waves, i.e. either (4.17) for TS$_1$ or (4.19) for RW, is generally referred to the vortex-b-m method.

Comparisons of the interface morphology evolution between the experiment and the vortex-b-m method for both thick and thin layers are given in figures 8 and 9, respectively. As we can see, the vortex-b-m method well reproduces the deformation of thick layers from linear to nonlinear stages, indicating that the current vortex model effectively captures the primary driving mechanisms behind instability growth in thick layers. However, for thin layers, the predictions of the vortex-b-m method evidently deviate from the experimental results, particularly at late stages, as illustrated in figure 9. Notably, in the case of d20-IP, the prediction suggests an intersection of the two interfaces, which is physically implausible. This discrepancy arises because the vortex-b-m method does not account for interface coupling effects, a crucial factor in the evolution of thin layers, as discussed in § 3.

### 4.4. *Involving interface coupling effect*

Under the assumption of incompressible, irrotational flow, the influence of interface coupling on instability growth in the linear regime has been theoretically analysed by Mikaelian (1995, 2005). However, extending these theoretical models to the nonlinear stage is challenging, as nonlinearity greatly increases the complexity of the problem. In



https://doi.org/10.1017/jfm.2025.178 Published online by Cambridge University Press

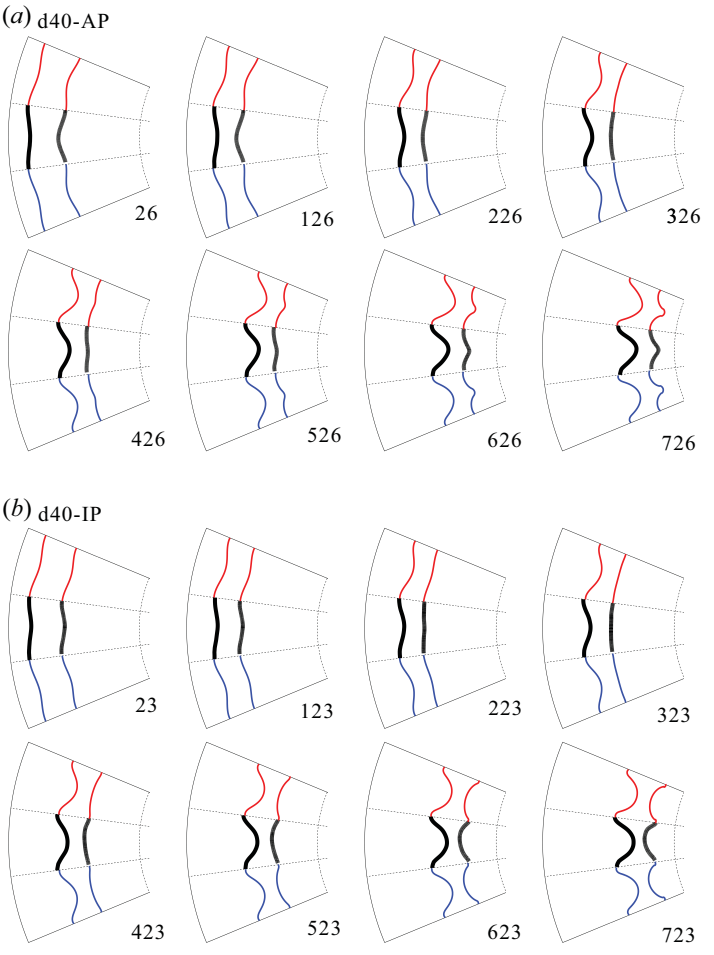



Figure 8. Comparison of the interface profile among the experiment (bold black line in the middle of each image), the vortex-b-m model (blue line at the bottom), and the vortex-b-m-c model (red line at the top) for cases d40-AP and d40-IP. The unit of numbers is μs.

particular, during the nonlinear stage of convergent RM instability, interface coupling effect could interact with other factors, such as geometric contraction and reverberating waves, further complicating the problem. So far, the influence of interface coupling on instability growth at the nonlinear stage, whether in planar or cylindrical geometry, has not been fully assessed. Unlike existing models, the vortex method can straightforwardly incorporate the effects of interface coupling by simultaneously considering the motion and transport of multiple vortex sheets at each time step. Considering this, the Lagrangian velocity of a fluid point at either interface is influenced by all the vortex sheets:

$$u - iv = \frac{i}{2\lambda}\left(\int_{S_1} + \int_{S_2} + \ldots + \int_{S_N}\right)\gamma' \cot\frac{\pi(z-z')}{\lambda}\mathrm{d}s'. \tag{4.20}$$

In the equation above, the integral path for each vortex sheet (e.g. $S_1$, $S_2$) is defined along the sheet itself, encompassing all Lagrangian points on that sheet. In the absence



https://doi.org/10.1017/jfm.2025.178 Published online by Cambridge University Press

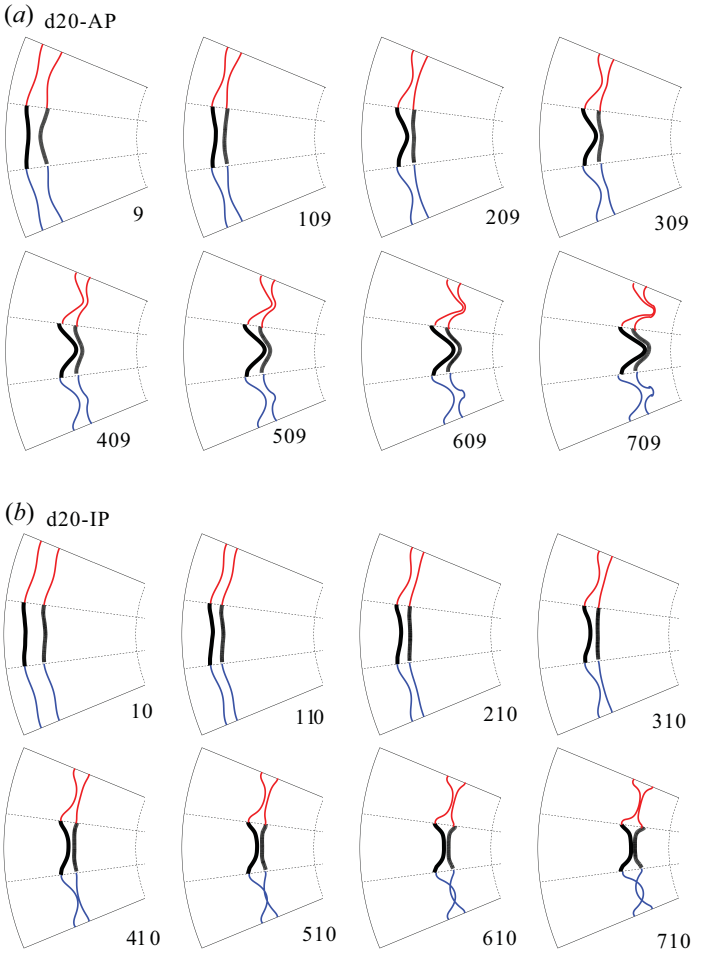



Figure 9. Comparison of the interface profile among the experiment (bold black line in the middle of each image), the vortex-b-m model (blue line at the bottom), and the vortex-b-m-c model (red line at the top) for cases d20-AP and d20-IP. The unit of numbers is μs.

of interface coupling effects, the velocity of any point on a vortex sheet is determined solely by integrating along that sheet. For example, the velocity of a point on $S_1$ would only require integration over $S_1$. However, when interface coupling is considered, the velocity calculation must account for contributions from all vortex sheets. For instance, in the double-interface configuration studied in our experiments, the velocity of a point on the inner interface $S_1$ is calculated as the sum of (i) the self-induced velocity obtained by integrating over all points on $S_1$ and (ii) the induced velocity from the outer interface obtained by integrating over all points on $S_2$. The vortex method adopting (4.20) is referred to as the vortex-b-m-c method.

Comparisons of the layer morphology evolution among the experiment, the vortex-b-m method and the vortex-b-m-c method for thick and thin layers are presented in figures 8 and 9, respectively. For thick layers, both vortex methods yield nearly identical predictions due to the weak interface coupling there. However, for thin layers, the vortex-b-m-c method provides significantly better predictions compared with the vortex-b-m method.



https://doi.org/10.1017/jfm.2025.178 Published online by Cambridge University Press

Particularly, at late stages when the two interfaces are nearly merging, the vortex-b-m-c method provides a more accurate prediction of the interface behaviour. The good agreement between the experiment and the vortex-b-m-c method highlights the significant role of interface coupling in the evolution of thin layers. As seen in figure 9, the vortex-b-m method exhibits a small roll-up at the late stage in the d20-AP case (709 μs), which is not observed in either the experiment or the prediction of the vortex-b-m-c method. This suggests that interface coupling inhibits the formation of roll-ups in an anti-phase layer. Additionally, the predicted interface morphology tends to be flatter (with smaller amplitude) for the IP case compared with the SU or US cases, while it shows a sharper structure (with larger amplitude) for the AP case. This observation is qualitatively consistent with the analysis of interface coupling at the linear stage of cylindrical RM instability (Mikaelian 2005).

Quantitative comparisons in the amplitude growths of the inner and outer interfaces among the experiment, the vortex-b-m method, and the vortex-b-m-c method are given in figure 10. For thick layers, both vortex methods provide reasonable predictions of instability growth, albeit with varying degrees of accuracy. Notably, for case d40-IP, the vortex-b-m method shows better agreement with experimental data for the outer interface compared with the vortex-b-m-c method, as shown in figure 10(*a*). This discrepancy can be attributed to two main factors. First, the vortex-b-m-c method assumes incompressible flow, where vorticity information propagates instantaneously between interfaces. However, in real flows, vorticity disturbances propagate at the speed of sound. For thick layers with widely separated interfaces, the time required for vorticity disturbance propagation becomes significant. As a result, the vortex-b-m-c method may overestimate the suppression effect for IP cases, as the actual coupling between distant interfaces is weaker than the model assumes. Second, despite the careful design of the experimental set-up, unavoidable factors such as the presence of thin filaments used to form the interfaces and three-dimensional effects may introduce measurement inaccuracies. These experimental uncertainties could make the simpler vortex-b-m method appear more accurate in some cases. In contrast, for thin layers where interfaces are sufficiently close, the vorticity propagation time is negligible, approximately satisfying the incompressible assumption, and coupling effects are strong enough to outweigh experimental uncertainties. Consequently, the vortex-b-m-c method consistently provides better predictions than the vortex-b-m method, particularly at late stages. These observations underscore the importance of considering compressibility effects when modelling interface coupling in instability growth. Despite this, to the authors' knowledge, this is the first accurate prediction of convergent RM instability at multiple interfaces across both linear and nonlinear stages. The present results exhibit great potential of the developed vortex method for studying the RM instability with complex physical factors such as geometric contraction, interface coupling and wave effects.

The present vortex method demonstrates excellent predictive capability for the majority of our experimental conditions. Nevertheless, it is important to emphasise that its validity is bounded by specific physical assumptions. Specifically, this method is based on the assumptions of incompressible, irrotational and inviscid flow, as well as an idealised point vortex approximation. These assumptions are consistent with the conditions of weak shocks and discontinuous interfaces in our experiments. However, the vortex method requires further refinement to address a broader range of conditions. For instance, under strong shock conditions, the effects of compressibility and bulk vorticity become significant (Wouchuk & Nishihara 1997) and must be accounted for. Similarly, for diffusive interfaces, the use of vortex kernel distributions should be considered instead of relying



https://doi.org/10.1017/jfm.2025.178 Published online by Cambridge University Press

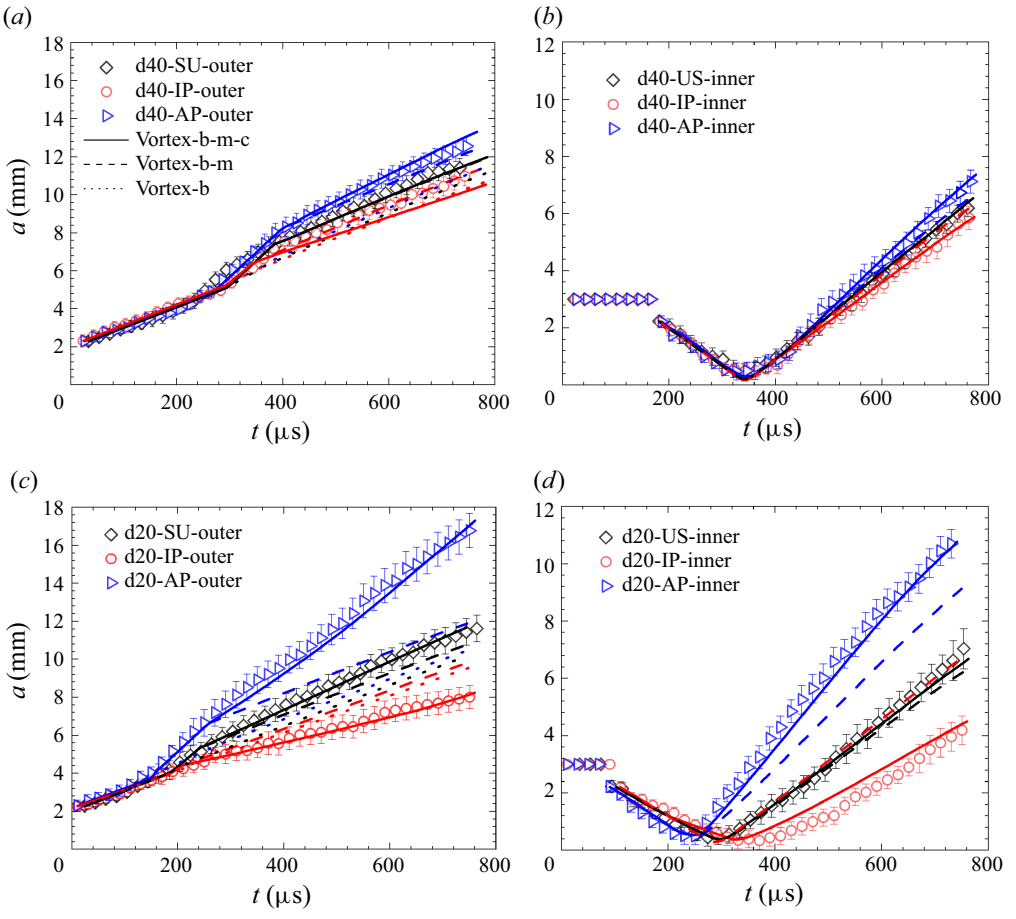



Figure 10. Comparison of the amplitudes of the (*a*,*c*) outer and (*b*,*d*) inner interfaces between experiments and predictions for layers of various thicknesses and shapes. The dotted line refers to the prediction of vortex-b model, the dashed line to the prediction of vortex-b-m and the solid line to the prediction of the vortex-b-m-c model. Note the predictions of the vortex-b method for instability growth at the inner interface of thin layers nearly collapse with the prediction of vortex-b-m for case d20-US, and thus are not shown in (*d*).

on the idealised point vortex approximation. Moreover, the current implementation of our vortex method requires experimental inputs for the background flow and initial growth rates. This seems to limit its direct application to cases without experimental data. However, we would like to clarify several points. First, the requirement of experimental inputs is not a fundamental limitation of the method itself, but rather a practical choice in the current implementation. The background flow could alternatively be obtained from theoretical analysis or numerical simulations. Second, for simple configurations where analytical solutions exist for initial growth rate and background flow (e.g. single-mode RM instability in planar geometry), our method can directly use these solutions without requiring experimental inputs. The need for experimental data primarily arises in convergent geometry where exact analytical solutions are currently unavailable. Third, the main contribution of our work is demonstrating how various physical effects (background flow, interface coupling, reverberating waves) can be incorporated into the vortex method framework. This framework can be adapted to other configurations by modifying the input parameters accordingly.



https://doi.org/10.1017/jfm.2025.178 Published online by Cambridge University Press

## 5. Conclusions

This work presents high-fidelity experiments on the convergent RM instability at an $SF_6$ layer surrounded by air using a novel convergent shock tube. The shock tube possesses a smoothly curved concave–oblique–convex wall profile designed based on shock dynamics theory. The curved wall first transforms an incident planar shock into a cylindrical one, then to a stronger planar shock that subsequently exits the end of the tube. This design effectively prevents shock focusing and reflection at the geometric centre, thereby significantly mitigating interface deceleration and the second impact of the reflected shock, which were unavoidable in previous experiments. Benefiting from this, long-term observation of convergent RM instability is achieved.

An unperturbed $SF_6$ surrounded by air, subjected to a cylindrical shock, is first examined to obtain the unsteady background flow in convergent RM instability. Then, various types of $SF_6$ layers with controllable thicknesses and shapes are examined. It is found that reverberating waves inside the layer significantly influence instability growth at the early stage, while interface coupling becomes the dominant factor at late stages. For thick layers, the evolutions of the outer and inner interfaces are nearly decoupled regardless of the layer shape. As a result, the weakly nonlinear model of Wang *et al.* (2015), designed for cylindrical RM instability at a single interface, accurately predicts instability growth at the inner interface for all cases. Nevertheless, it slightly underestimates instability growth at the outer interface, as the rarefaction wave reflected from the inner interface modestly enhances the outer interface evolution. For thin layers, interface coupling becomes more pronounced, and instability growth is influenced by both reverberating waves and interface coupling, each of which is highly sensitive to the layer shape. It is found that the perturbation growth at either the outer or inner interface is fastest in the layer with initial anti-phase perturbations, moderate in the layer with only one initial perturbed interface and slowest in the layer with initial in-phase perturbations. The vortex method, originally developed for KH and RT instabilities, is extended to the convergent RM instability by incorporating the influences of unsteady background flow into the transport equation of vortex sheet strength. Within the vortex method framework, the effects of interface coupling and reverberating waves can be straightforwardly incorporated. The extended vortex method shows good agreement with experimental results, exhibiting its significant potential for studying the RM instability under complex physical conditions. In the near future, this vortex method will be applied to the RM instability at multi-mode interfaces and in divergent geometries. The finding in this work provides a guideline for modulating the instability growth rate in convergent RM instability at multiple interfaces, which is essential for optimising target design in ICF. The vortex approach developed represents a novel way to predict convergent RM instability at multiple interfaces across both linear and nonlinear stages.

**Funding.** This work was supported by the National Natural Science Foundation of China (nos 12388101, 12402259), the National Key Research and Development Program of China (2022YFF0504500), the Strategic Priority Research Program of Chinese Academy of Science (XDB1100120, XDB0500301) and Laoshan Laboratory (LSKJ202300305).

**Declaration of interests.** The authors report no conflict of interest.

## Appendix

In this appendix, the primary governing equations of the original vortex method are reviewed, which serve as the basis for deriving the vortex method for convergent RM instability.



https://doi.org/10.1017/jfm.2025.178 Published online by Cambridge University Press

For shear flows such as RT and KH instabilities, the circulation along an interface (or a velocity discontinuity) can be computed using the following formula:

$$\Gamma = \int \gamma(s)\mathrm{d}s, \tag{A1}$$

where $s$ is the arclength coordinate along the interface and $\gamma$ is the vortex sheet strength, defined as the jump in tangential velocity across the interface,

$$\gamma = (\boldsymbol{u}_1 - \boldsymbol{u}_2)\cdot\boldsymbol{s}. \tag{A2}$$

Here, $\boldsymbol{u_1}$ and $\boldsymbol{u_2}$ are the velocities on either side of the interface and $\boldsymbol{s}$ is the unit tangent vector at the interface. A crucial step of the vortex method is developing a transport equation for the vortex sheet strength. With this in mind, we start with the basic conservation laws. For an interface between two incompressible, irrotational and inviscid fluids, the flow on each side of the interface follows the Euler equation:

$$\boldsymbol{a}_i = -\frac{1}{\rho_i}\nabla p_i - \boldsymbol{g}, \quad i = 1, 2, \tag{A3}$$

where $\boldsymbol{a}$ is the acceleration of a fluid point, $\rho$ is the density, $p$ is the pressure and $\boldsymbol{g}$ is the body force per unit mass (typically referring to the gravitational acceleration).

Subtracting the tangential component of (A3) across the interface, we obtain

$$(\boldsymbol{a}_1 - \boldsymbol{a}_2)\cdot\boldsymbol{s} = A(\boldsymbol{a}_1 + \boldsymbol{a}_2)\cdot\boldsymbol{s} + 2A\boldsymbol{g}\cdot\boldsymbol{s} - \frac{2}{\rho_1+\rho_2}\frac{\partial\,(p_1 - p_2)}{\partial s}, \tag{A4}$$

where $A$ is the Atwood number defined previously. The acceleration of a fluid point can be reformulated as

$$\boldsymbol{a}_i = \frac{\partial \boldsymbol{u}_i}{\partial t} + \boldsymbol{U}\cdot\nabla\boldsymbol{u}_i \pm \frac{1}{2}\gamma\frac{\partial \boldsymbol{u}_i}{\partial s}, \tag{A5}$$

where $\boldsymbol{U} = (\boldsymbol{u}_1 + \boldsymbol{u}_2)/2$ denotes the Lagrangian velocity of the interface, and the $+$ $(-)$ sign is for $i = 1$ (2). Substituting (A5) into (A4), a transport equation for the vortex sheet strength is obtained:

$$\frac{\mathrm{d}\gamma}{\mathrm{d}t} + \gamma\frac{\partial \boldsymbol{U}}{\partial s}\cdot\boldsymbol{s} = 2A\left(\frac{\mathrm{d}\boldsymbol{U}}{\mathrm{d}t}\cdot\boldsymbol{s} + \frac{1}{8}\frac{\partial\gamma^2}{\partial s}\right) + 2A\boldsymbol{g}\cdot\boldsymbol{s} - \frac{2}{\rho_1+\rho_2}\frac{\partial\,(p_1 - p_2)}{\partial s}. \tag{A6}$$

The pressure difference across the interface satisfies the Laplace's equation, $p_1 - p_2 = \sigma(1/R)$, with $\sigma$ being the surface tension coefficient and $R$ being the radius of curvature.

## References


Baker, G.R., Meiron, D.I. & Orszag, S.A. 1980 Vortex simulations of the Rayleigh–Taylor instability. *Phys. Fluids* **23** (5), 1485–1490.

Baker, G.R., Meiron, D.I. & Orszag, S.A. 1982 Generalized vortex methods for free-surface flow problems. *J. Fluid Mech.* **123**, 477–501.

Bates, J.W. 2012 On the theory of a shock wave driven by a corrugated piston in a non-ideal fluid. *J. Fluid Mech.* **691**, 146–164.

Bell, G.I. 1951 Taylor instability on cylinders and spheres in the small amplitude approximation. *Tech. Rep.* LA-1321. LANL Los Alamos Scientific Laboratory of the University of California.

Betti, R. & Hurricane, O.A. 2016 Inertial-confinement fusion with lasers. *Nat. Phys.* **12** (5), 435–448.

Biamino, L., Jourdan, G., Mariani, C., Houas, L., Vandenboomgaerde, M. & Souffland, D. 2015 On the possibility of studying the converging Richtmyer–Meshkov instability in a conventional shock tube. *Exp. Fluids* **56** (2), 1–5.

Brouillette, M. 2002 The Richtmyer–Meshkov instability. *Annu. Rev. Fluid Mech.* **34** (1), 445–468.

Calvo-Rivera, A., Huete, C. & Velikovich, A.L. 2022 The stability of expanding reactive shocks in a van der Waals fluid. *Phys. Fluids* **34** (4), 046106.




https://doi.org/10.1017/jfm.2025.178 Published online by Cambridge University Press

CALVO-RIVERA, A., VELIKOVICH, A.L. & HUETE, C. 2023 Stability of expanding accretion shocks for an arbitrary equation of state. *J. Fluid Mech.* **964**, A33.

COHEN, R.D. 1991 Shattering of a liquid drop due to impact. *Proc. R. Soc. Lond. A* **435**, 483–503.

DELL, Z.R., PANDIAN, A., BHOWMICK, A.K., SWISHER, N.C., STANIC, M., STELLINGWERF, R.F. & ABARZHI, S.I. 2017 Maximum initial growth-rate of strong-shock-driven Richtmyer–Meshkov instability. *Phys. Plasmas* **24** (9), 090702.

DING, J., LI, J., SUN, R., ZHAI, Z. & LUO, X. 2019 Convergent Richtmyer–Meshkov instability of a heavy gas layer with perturbed outer interface. *J. Fluid Mech.* **878**, 277–291.

DING, J., SI, T., CHEN, M., ZHAI, Z., LU, X. & LUO, X. 2017*a* On the interaction of a planar shock with a three-dimensional light gas cylinder. *J. Fluid Mech.* **828**, 289–317.

DING, J., SI, T., YANG, J., LU, X., ZHAI, Z. & LUO, X. 2017*b* Measurement of a Richtmyer–Meshkov instability at an air-$SF_6$ interface in a semiannular shock tube. *Phys. Rev. Lett.* **119** (1), 014501.

FINCKE, J.R., LANIER, N.E., BATHA, S.H., HUECKSTAEDT, R.M., MAGELSSEN, G.R., ROTHMAN, S.D., PARKER, K.W. & HORSFIELD, C.J. 2004 Postponement of saturation of the Richtmyer–Meshkov instability in a convergent geometry. *Phys. Rev. Lett.* **93** (11), 115003.

GONCHAROV, V.N. 2002 Analytical model of nonlinear, single-mode, classical Rayleigh–Taylor instability at arbitrary Atwood numbers. *Phys. Rev. Lett.* **88** (13), 134502.

GROOM, M. & THORNBER, B. 2021 Reynolds number dependence of turbulence induced by the Richtmyer–Meshkov instability using direct numerical simulations. *J. Fluid Mech.* **908**, A31.

DE HENRY, F.M.T., MOVAHED, P. & JOHNSEN, E. 2014 Numerical simulations of a shock interacting with successive interfaces using the Discontinuous Galerkin method: the multilayered Richtmyer–Meshkov and Rayleigh–Taylor instabilities. *Shock Waves* **25** (4), 329–345.

HOSSEINI, S.H.R. & TAKAYAMA, K. 2005 Experimental study of Richtmyer–Meshkov instability induced by cylindrical shock waves. *Phys. Fluids* **17** (8), 084101.

HUETE, C., VELIKOVICH, A.L., MARTÍNEZ-RUIZ, D. & CALVO-RIVERA, A. 2021 Stability of expanding accretion shocks for an arbitrary equation of state. *J. Fluid Mech.* **927**, A35.

ISHIZAKI, R., NISHIHARA, K., SAKAGAMI, H. & UESHIMA, Y. 1996 Instability of a contact surface driven by a nonuniform shock wave. *Phys. Rev.* E **53** (6), R5592–R5595.

JACOBS, J.W., JENKINS, D.G., KLEIN, D.L. & BENJAMIN, R.F. 1995 Nonlinear growth of the shock-accelerated instability of a thin fluid layer. *J. Fluid Mech.* **295** (1), 23–42.

KRASNY 1986 Desingularization of periodic vortex sheet roll-up. *J. Comput. Phys.* **65**, 292–313.

LANIER, N.E., BARNES, C.W., BATHA, S.H., DAY, R.D., MAGELSSEN, G.R., SCOTT, J.M., DUNNE, A.M., PARKER, K.W. & ROTHMAN, S.D. 2003 Multimode seeded Richtmyer–Meshkov mixing in a convergent, compressible, miscible plasma system. *Phys. Plasmas* **10** (5), 1816–1821.

LEI, F., DING, J., SI, T., ZHAI, Z. & LUO, X. 2017 Experimental study on a sinusoidal air/$SF_6$ interface accelerated by a cylindrically converging shock. *J. Fluid Mech.* **826**, 819–829.

LI, J., DING, J., LUO, X. & ZOU, L. 2022 Instability of a heavy gas layer induced by a cylindrical convergent shock. *Phys. Fluids* **34** (4), 042123.

LI, J., DING, J., SI, T. & LUO, X. 2020 Convergent Richtmyer–Meshkov instability of light gas layer with perturbed outer surface. *J. Fluid Mech.* **884**, R2.

LI, X., FU, Y., YU, C. & LI, L. 2021 Statistical characteristics of turbulent mixing in spherical and cylindrical converging Richtmyer–Meshkov instabilities. *J. Fluid Mech.* **928**, A10.

LIANG, Y. & LUO, X. 2021 On shock-induced heavy-fluid-layer evolution. *J. Fluid Mech.* **920**, A13.

LIGRANI, P.M., MCNABB, E.S., COLLOPY, H., ANDERSON, M. & MARKO, S.M. 2020 Recent investigations of shock wave effects and interactions. *Adv. Aerodyn.* **2** (1), 4.

LINDL, J., LANDEN, O., EDWARDS, J., MOSES, E. & TEAM, N. 2014 Review of the national ignition campaign 2009–2012. *Phys. Plasmas* **21** (2), 020501.

LIU, L., LIANG, Y., DING, J., LIU, N. & LUO, X. 2018 An elaborate experiment on the single-mode Richtmyer–Meshkov instability. *J. Fluid Mech.* **853**, R2.

LIU, W.H., HE, X.T. & YU, C.P. 2012 Cylindrical effects on Richtmyer–Meshkov instability for arbitrary Atwood numbers in weakly nonlinear regime. *Phys. Plasmas* **19** (7), 072108.

LIU, W.H., YU, C.P., YE, W.H., WANG, L.F. & HE, X.T. 2014 Nonlinear theory of classical cylindrical Richtmyer–Meshkov instability for arbitrary Atwood numbers. *Phys. Plasmas* **21** (6), 062119.

LOMBARDINI, M., PULLIN, D.I. & MEIRON, D.I. 2014*a* Turbulent mixing driven by spherical implosions. Part 1. Flow description and mixing-layer growth. *J. Fluid Mech.* **748**, 85–112.

LOMBARDINI, M., PULLIN, D.I. & MEIRON, D.I. 2014*b* Turbulent mixing driven by spherical implosions. Part 2. Turbulence statistics. *J. Fluid Mech.* **748**, 113–142.

LUO, X., DING, J., WANG, M., ZHAI, Z. & SI, T. 2015 A semi-annular shock tube for studying cylindrically converging Richtmyer–Meshkov instability. *Phys. Fluids* **27** (9), 091702.



https://doi.org/10.1017/jfm.2025.178 Published online by Cambridge University Press

LUO, X., LI, M., DING, J., ZHAI, Z. & SI, T. 2019 Nonlinear behaviour of convergent Richtmyer–Meshkov instability. *J. Fluid Mech.* **877**, 130–141.
LUO, X., ZHANG, F., DING, J., SI, T., YANG, J., ZHAI, Z. & WEN, C. 2018 Long-term effect of Rayleigh–Taylor stabilization on converging Richtmyer–Meshkov instability. *J. Fluid Mech.* **849**, 231–244.
MESHKOV, E.E. 1969 Instability of the interface of two gases accelerated by a shock wave. *Fluid Dyn.* **4** (5), 101–104.
MIKAELIAN, K.O. 1995 Rayleigh–Taylor and Richtmyer–Meshkov instabilities in finite-thickness fluid layers. *Phys. Fluids* **7** (4), 888–890.
MIKAELIAN, K.O. 2005 Rayleigh–Taylor and Richtmyer–Meshkov instabilities and mixing in stratified cylindrical shells. *Phys. Fluids* **17** (9), 094105.
MOHAGHAR, M., CARTER, J., PATHIKONDA, G. & RANJAN, D. 2019 The transition to turbulence in shock-driven mixing: effects of Mach number and initial conditions. *J. Fluid Mech.* **871**, 595–635.
PENG, N., YANG, Y., WU, J. & XIAO, Z. 2021 Mechanism and modelling of the secondary baroclinic vorticity in the Richtmyer–Meshkov instability. *J. Fluid Mech.* **911**, A56.
PFAFF, T., THUEREY, N. & GROSS, M. 2012 Lagrangian vortex sheets for animating fluids. *ACM Trans. Graph.* **31** (4), 1–8.
PLESSET, M.S. 1954 On the stability of fluid flows with spherical symmetry. *J. Appl. Phys.* **25** (1), 96–98.
RANJAN, D., NIEDERHAUS, J.H.J., OAKLEY, J.G., ANDERSON, M.H., BONAZZA, R. & GREENOUGH, J.A. 2008 Shock-bubble interactions: features of divergent shock-refraction geometry observed in experiments and simulations. *Phys. Fluids* **20** (3), 036101.
RANJAN, D., OAKLEY, J. & BONAZZA, R. 2011 Shock-bubble interactions. *Annu. Rev. Fluid Mech.* **43** (1), 117–140.
RAYLEIGH, L. 1883 Investigation of the character of the equilibrium of an incompressible heavy fluid of variable density. *Proc. Lond. Math. Soc* **14**, 170–177.
RICHTMYER, R.D. 1960 Taylor instability in shock acceleration of compressible fluids. *Commun. Pure Appl. Maths* **13** (2), 297–319.
RYU, D. & VISHNIAC, E.T. 1987 The growth of linear perturbations of adiabatic shock waves. *Astrophys. J.* **313**, 820–841.
SAMTANEY, R., RAY, J. & ZABUSKY, N.J. 1998 Baroclinic circulation generation on shock accelerated slow/fast gas interfaces. *Phys. Fluids* **10** (5), 1217–1230.
SAMTANEY, R. & ZABUSKY, N.J. 1994 Circulation deposition on shock-accelerated planar and curved density-stratified interfaces: models and scaling laws. *J. Fluid Mech.* **269**, 45–78.
SOHN, S.I. 2003 Simple potential-flow model of Rayleigh–Taylor and Richtmyer–Meshkov instabilities for all density ratios. *Phys. Rev.* E **67** (2), 026301.
SOHN, S.-I. 2011 Late-time vortex dynamics of Rayleigh–Taylor Instability. *J. Phys. Soc. Japan* **80** (8), 084401.
SOHN, S.I., YOON, D. & HWANG, W. 2010 Long-time simulations of the Kelvin-Helmholtz instability using an adaptive vortex method. *Phys. Rev.* E **82** (4), 046711.
STANIC, M., STELLINGWERF, R.F., CASSIBRY, J.T. & ABARZHIS, I. 2012 Scale coupling in Richtmyer–Meshkov flows induced by strong shocks. *Phys. Plasmas* **19** (9), 082706.
TAYLOR, G. 1950 The instability of liquid surfaces when accelerated in a direction perpendicular to their planes. I. *Proc. R. Soc. Lond.* A: *Math. Phys. Sci.* **201** (1065), 192–196.
TRYGGVASON, G. 1988 Numerical simulations of the Rayleigh–Taylor instability. *J. Comput. Phys.* **75** (2), 253–282.
URZAY, J. 2018 Supersonic combustion in air-breathing propulsion systems for hypersonic flight. *Annu. Rev. Fluid Mech.* **50** (1), 593–627.
VANDENBOOMGAERDE, M., ROUZIER, P., SOUFFLAND, D., BIAMINO, L., JOURDAN, G., HOUAS, L. & MARIANI, C. 2018 Nonlinear growth of the converging Richtmyer–Meshkov instability in a conventional shock tube. *Phys. Rev. Fluids* **3** (1), 014001.
VELIKOVICHA, A.L. 1996 Analytic theory of Richtmyer–Meshkov instability for the case of reflected rarefaction wave. *Phys. Fluids* **8** (6), 1666–1679.
VISHNIAC, E.T. 1983 The dynamic and gravitational instabilities of spherical shocks. *Astrophys. J.* **274**, 152–167.
WANG, H., WANG, H., ZHAI, Z. & LUO, X. 2023 High-amplitude effect on single-mode Richtmyer–Meshkov instability of a light–heavy interface. *Phys. Fluids* **35** (1), 016106.
WANG, L.F., WU, J.F., GUO, H.Y., YE, W.H., LIU, J., ZHANG, W.Y. & HE, X.T. 2015 Weakly nonlinear Bell-Plesset effects for a uniformly converging cylinder. *Phys. Plasmas* **22** (8), 082702.
WOUCHUK, J.G. & NISHIHARA, K. 1997 Asymptotic growth in the linear Richtmyer–Meshkov instability. *Phys. Plasmas* **4** (4), 1028–1038.

https://doi.org/10.1017/jfm.2025.178 Published online by Cambridge University Press

Wu, Z., Li, Y., Lu, L., Xu, X. & liang, R. 2024 Influence of the shock wave-turbulence interaction on the swirl distortion in hypersonic inlet. *Adv. Aerodyn.* **6** (1), 23.

Xu, J., Wang, H., Zhai, Z. & Luo, X. 2023 Convergent Richtmyer–Meshkov instability on two-dimensional dual-mode interfaces. *J. Fluid Mech.* **965**, A8.

Yan, Z., Fu, Y., Wang, L., Yu, C., Li, X. 2022 Effect of chemical reaction on mixing transition and turbulent statistics of cylindrical Richtmyer–Meshkov instability. *J. Fluid Mech.* **941**, A55.

Yang, Y., Zhang, Q. & Sharp, D.H. 1994 Small amplitude theory of Richtmyer–Meshkov instability. *Phys. Fluids* **6** (5), 1856–1873.

Zhai, Z., Liu, C., Qin, F., Yang, J. & Luo, X. 2010 Generation of cylindrical converging shock waves based on shock dynamics theory. *Phys. Fluids* **22** (4), 041701.

Zhan, D., Li, Z., Yang, J., Zhu, Y. & Yang, J. 2018 Note: A contraction channel design for planar shock wave enhancement. *Rev. Sci. Instrum.* **89** (5), 056104.

Zhang, D., Ding, J., Li, M., Zou, L. & Luo, X. 2023*a* Effects of reverberating waves and interface coupling on a divergent Richtmyer–Meshkov instability. *J. Fluid Mech.* **975**, A44.

Zhang, D., Ding, J., Si, T. & Luo, X. 2023*b* Divergent Richtmyer–Meshkov instability on a heavy gas layer. *J. Fluid Mech.* **959**, A37.

Zhang, Q., Deng, S. & Guo, W. 2018*a* Quantitative theory for the growth rate and amplitude of the compressible Richtmyer–Meshkov instability at all density ratios. *Phys. Rev. Lett.* **121** (17), 174502.

Zhang, Q. & Sohn, S.I. 1997 Nonlinear theory of unstable fluid mixing driven by shock wave. *Phys. Fluids* **9** (4), 1106–1124.

Zhang, W., Wu, Q., Zou, L., Zheng, X., Li, X., Luo, X. & Ding, J. 2018*b* Mach number effect on the instability of a planar interface subjected to a rippled shock. *Phys. Rev. E* **98** (4), 043105.

Zhang, Y., Zhao, Y., Ding, J. & Luo, X. 2023*c* Richtmyer–Meshkov instability with a rippled reshock. *J. Fluid Mech.* **968**, A3.

Zhou, Y. 2017*a* Rayleigh–Taylor and Richtmyer–Meshkov instability induced flow, turbulence, and mixing. I. *Phys. Rep.* **720-722**, 1–136.

Zhou, Y. 2017*b* Rayleigh–Taylor and Richtmyer–Meshkov instability induced flow, turbulence, and mixing. II. *Phys. Rep.* **723-725**, 1–160.

Zou, L., Al-Marouf, M., Cheng, W., Samtaney, R., Ding, J. & Luo, X. 2019 Richtmyer–Meshkov instability of an unperturbed interface subjected to a diffracted convergent shock. *J. Fluid Mech.* **879**, 448–467.

https://doi.org/10.1017/jfm.2025.178 Published online by Cambridge University Press